Available online at www.sciencedirect.com

ScienceDirect

Advances in Space Research xxx (xxxx) xxx

ADVANCES IN SPACE RESEARCH (a COSPAR publication)

www.elsevier.com/locate/asr

Considerations of VLBI transmitters on Galileo satellites

Ahmad Jaradat [a,*], Frederic Jaron [a,b,c], Jakob Gruber [c], Axel Nothnagel [a,c]

[a] Institute of Geodesy and Geoinformation, University of Bonn, Nußallee 17, DE-53115 Bonn, Germany
[b] Chalmers University of Technology, Onsala Space Observatory, SE-412 96 Onsala, Sweden
[c] Technische Universität Wien, Department für Geodäsie und Geoinformation, Wiedner Hauptstraße 8, A-1040 Wien, Austria

Received 19 November 2020; received in revised form 29 April 2021; accepted 30 April 2021

Abstract

For directly linking the dynamical reference frame of satellite orbits to the quasi-inertial reference frame of extra-galactic radio sources, observations of satellites with the Very Long Baseline Interferometry (VLBI) technique are the only conceivable method. Hence, the satellite observations should be embedded in VLBI network sessions during which also natural radio sources are observed. For this reason, it would be most practical if the artificial signal generated at the satellite for VLBI observations covers the same frequency bands as regularly observed by VLBI radio telescopes and should have a similar flux density across the observed bandwidth as these natural sources. The use of satellites of Global Navigation Satellite Systems (GNSS) such as the Galileo system is advisable because they are well monitored in terms of precise orbit determination and the altitude allows common visibilities of many VLBI telescopes. So far, signal generation on a GNSS satellite dedicated to VLBI observations has not been realized yet, partly because suitable signal generation equipment has not been considered in depth. In addition, many aspects, such as legal implications and technical complications, have not yet been addressed. In this publication, we compiled various aspects of generating an artificial VLBI signal on a GNSS satellite. We describe the legal and technical aspects of generating and emitting an artificial signal on a Galileo satellite suitable for VLBI observations including a design study for the necessary equipment on the satellite. Since geodetic VLBI is currently in a transition period from traditional observations at S and X band to the broadband VLBI Global Observing System (VGOS), the proposed equipment generates a signal suitable for both frequency setups. We have also considered the restrictions for installation on a satellite, such as power consumption, weight, and size. The equipment mainly consists of three devices: noise source, amplifier, and antenna. A diode is used as the noise source. This noise is amplified by a set of low noise amplifiers and then radiated by a spiral antenna. The diode and the amplifiers were chosen from the market, but the antenna was newly designed and simulated. The output signal of this chain was tested using a VLBI baseband data simulator, then correlated and fringe-fitted for validation. The instrumentation proposed here is easy to be constructed, but will still have to be tested in the laboratory together with the instruments on the actual satellite.

Keywords: Artificial VLBI signal generation; VLBI transmitter; Geodetic VLBI; VGOS; GNSS; Baseband simulator

1. Introduction

Reference systems play an important role in all kinds of astroscience and geoscience. Three categories need to be considered in this context. The celestial reference system (CRS) is realized by the positions of compact extra-galactic radio sources, predominantly quasars, e.g., in the International Celestial Reference Frame (ICRF), with the latest official solution ICRF3 (Charlot et al., 2020). The

* Corresponding author at: University of Tasmania, Private Bag 37, 7001 Hobart, Australia.
E-mail addresses: Ahmad.Jaradat@utas.edu.au (A. Jaradat), frederic.jaron@tuwien.ac.at (F. Jaron), jakob.franz.gruber@tuwien.ac.at (J. Gruber), axel.nothnagel@tuwien.ac.at (A. Nothnagel).

https://doi.org/10.1016/j.asr.2021.04.048
0273-1177/

terrestrial reference system (TRS) is realized by precise coordinates of space-geodetic observing instruments, e.g., as the International Terrestrial Reference Frame (ITRF), with ITRF2014 as the latest official solution (Altamimi et al., 2016). And finally, a variety of dynamic reference systems (DRS) are realized by the orbits of artificial Earth satellites, predominantly satellites of Global Navigation Satellite Systems (GNSS). For various reasons, such as for the detection and elimination of systematics between the different observing techniques, it is important that these reference systems are linked with each other with high accuracy and consistency (Rothacher et al., 2009).

While the TRS is very well linked with the CRS and to various DRS through observing instruments, such as satellite receivers and antennas, the link between the CRS and the DRS is currently only materialized through indirect methods making use of local ties on Earth between the measurement instruments observing these objects, i.e., radio telescopes and receivers of GNSS. Since these ties exhibit systematic differences between techniques (Altamimi et al., 2016) it has been a long time goal to also establish ties between reference systems on the satellites, so-called space ties. To establish the ties between the CRS and the DRS, observations of satellites with VLBI radio telescopes preferably in front of the quasar background are the method of choice.

For this purpose, a number of activities have been initiated in this field within the geodetic VLBI community. Suitable satellite orbits and antenna networks were investigated (e.g., Plank, 2014; Plank et al., 2014). Scheduling and observing strategies for GNSS satellites were investigated and simulated to generate space ties (e.g., Plank, 2014), which included the development of a satellite mode for scheduling software (e.g., Hellerschmied et al., 2015). In a number of VLBI experiments, GNSS satellites were observed at L band with equipment existing at radio telescopes (e.g., Tornatore et al., 2011, 2014). However, at some of the radio telescopes this required modifying the S/X receivers, used during standard VLBI geodetic experiments, to also cover L band (e.g., Haas et al., 2014; McCallum et al., 2016). Moreover, Differential One-Way Ranging (DOR) tones were processed from observations of nano-satellites (e.g., Hellerschmied et al., 2016; Sun et al., 2018) or of the Chang'E-3 moon lander (e.g., Li et al., 2015; Klopotek et al., 2019) and subsequently, the necessary VLBI post-processing tools have been developed to handle this type of signal properly (e.g., Han et al., 2019; Hellerschmied et al., 2018). Since Earth satellites are in the near field of VLBI, the theoretical modeling of the delay requires special treatment (see Jaron and Nothnagel, 2019, and references therein). An example of a complete process chain from scheduling, observation, correlation, fringe-fitting, to final analysis was realized by Plank et al. (2017). Furthermore, extensive simulations were done to study the feasibility of employing geodetic VLBI for precise orbit determination of Earth-orbiting satellites (Klopotek et al., 2020).

Unfortunately, none of these endeavors brought a real breakthrough in terms of usability of these observations for real frame ties, and the current state of the art is limited to simulations (Männel, 2016; Anderson et al., 2018). One of the main reasons for the lack of success is that the artificial signals observed by the radio telescopes are rather limited in bandwidth and/or that the emitting antennas are not made for this purpose. It would therefore be ideal if these shortcomings are overcome and a dedicated chain of emission of a synthetic quasar signal would be deployed on a GNSS satellite. Particular emphasis should be put on the fact that the source of emission, i.e., the antenna, resembles a point source, which is also the requirement for ideal quasars in geodetic VLBI.

For this purpose, we have embarked on configuring the elements needed for such equipment but also because the use of such transmitters has been proposed already in other proposals such as GRASP (Bar-Sever et al., 2009) or E-GRASP (Biancale, 2016), though not funded at this stage. We chose the Galileo satellite constellation (also in the title) because for these, concrete specifications had been provided in an ESA call (European Space Agency, 2019). Of course, the ideas developed in this publication can be used in any future satellite system's payload designed for co-location of space-geodetic techniques.

We start the paper with briefly addressing a number of aspects of the whole concept, which are often forgotten when asking for development of such equipment (Section 2). In Sections 3–6 we describe the development of the system. At the end, in Section 7, we simulate the emission of the system as observed and recorded by ground-based telescopes and perform correlation and fringe-fitting for validation. We give our conclusions in Section 8.

2. Initial considerations and constraints

Before we start going into the technical details of the dedicated VLBI transmitter, we should also address some of the initial considerations, implications, and constraints. In general, it should be noted that more and more artificial radio signals from Earth orbiting satellites pollute the electromagnetic spectrum for radio astronomers. In the hunt for very remote astrophysical phenomena, radio astronomers use large radio telescopes with very sensitive receiving equipment at a variety of frequencies, often related to opacity windows of the atmosphere and emission lines of physical processes and chemical elements. Any additional artificial signal in the radio spectrum will disturb their observations and they are not too keen to see geodesists pushing for deployment of additional sources of radio frequency interferences (RFI). Developments, thus, have to be promoted very carefully and in close consultation with this neighboring discipline. In any case, one of the prerequisites of an artificial radio source resembling a quasar is that it can be switched off at any time when geodetic observations are not carried out.

The second point is that the International Telecommunication Union (ITU),[1] which is the responsible organization for issues related to worldwide information and communication technologies, has some clear restrictions on the use of radio frequency emission. The Radio Regulations (RR) of ITU (ITU, 2020) contains a few items which need to be considered. Most important is the limitation in power flux density at any angle of arrival to −213.3 dBW/m^2 at 4 kHz bandwidth (Chapter 6, article 21, Section 5). The second ITU issue is that sources of interference need to "furnish current ephemeral data necessary to allow determination of the positions" of the transmitter (Chapter 4, article 15, Section 6, point 25). Third, the transmitter needs a device "to ensure immediate cessation of their radio emissions by telecommand, whenever such cessation is required under the provisions of these Regulations" (Chapter 6, article 21, Section 1).

In handling all these issues, the national administrations play an important role which should not be forgotten. The proponent of the project (e.g., ESA) will also have to require a modification in the ITU filing for the frequency usage and beam shape of the antenna which should be filed under RR No 4.4 (no protection/no interference basis). This has to be accepted by the national administrations first. Opposition can be raised by, e.g., claiming that transmissions will interfere with certain services that have frequency allocations. As an additional aspect for ITU registration, the application of the VLBI transmitter could be considered as an Earth exploration-satellite service which is a passive and active service between space and Earth stations.

Concerning the frequencies to be observed for frame tie projects by geodetic radio telescopes, we have to consider the current situation and the future evolution of the observing network of the International VLBI Service for Geodesy and Astrometry (IVS, Nothnagel et al., 2017). At the time of writing, most telescopes of the IVS are configured for observations in X and S band, i.e., 8200–9000 MHz and 2200–2400 MHz, respectively, in the so-called legacy mode. Most of these telescopes have diameters of 20 m or more and mostly are not capable of doing satellite tracking straight away. This is only possible with dedicated tracking features with rapid incremental position updates requiring special scheduling mechanisms (Hellerschmied et al., 2016). The future IVS network, however, consists of very agile radio telescopes of the 12–13 m class, known as VGOS telescopes for populating the VLBI Global Observing System (VGOS, Niell et al., 2018) network. These are mostly equipped for satellite tracking already. Approximately ten of these telescopes are currently ramping up their operational readiness for observations in the broadband mode. Here, the configurations of the frontends (feed horn, receivers, and first stage of local oscillators) are prepared for covering the entire bandwidth of 2–14 GHz. Out of this band, four sub-bands of 512 MHz, and later of 1 GHz, each, are filtered, digitized and time-tagged for the standard VLBI processing chain (Nothnagel, 2018). The optimal location of the sub-bands is under investigation for simultaneous ionosphere estimation in the level-1 data analysis. An additional aspect in this context is the expected RFI from massive future satellite radiation stemming from Synthetic Aperture Radar Systems or the Starlink and OneWeb downlinks. They are considered to become a serious impairment for any VLBI observations.

With respect to RFI it should also be mentioned that this does not only affect the higher frequencies in the radio frequency spectrum used for VGOS. Also S band is highly corrupted by RFI in particular from ground-based transmitters such as Wifi, radio broadcasting, and mobile phone transmission. It is therefore critical to find undisturbed sub-bands in this spectrum as well.

Besides the problem of RFI originating from unrelated sources there is also the potential for disturbances by signals emitted from the GNSS satellite itself. In principle the GNSS signal could leak into the amplifier of the VLBI transmitter on the satellite. Another possibility is that out-of-band emission of the GNSS signal is observed by the radio telescopes in addition to the quasar-like signal when pointing at the satellite. However, in VLBI observations of GNSS satellites carried out so far, none such phenomena have been reported (Plank et al., 2017, and reference therein). In addition, modern digital filtering (e.g., notch filters) should be able to eliminate unwanted signal components. If the instrumentation proposed here is to be built, the exact emission spectrum has to be analyzed in the laboratory.

The two types of radio telescopes of the IVS, i.e., legacy and VGOS, observe in two entirely different polarizations, a fact which has some importance for the artificial signal generation chain as well. All S and X band feeds are configured for right circular polarization (RCP) in IEEE convention (Hamaker and Bregman, 1996), while the VGOS broadband feeds have two perpendicular linear polarizations. In the first case, a transmitting antenna on the satellite should thus produce a left circular polarization (LCP) to produce optimal gain of the system. In contrast to this, an ideal RCP antenna on the satellite would eliminate the gain entirely. For the VGOS receiving system, ideally an unpolarized transmission antenna should be mounted on the satellite. However, since this is not possible a circular polarized antenna would be the choice here as well. To keep this consistent with a setup for legacy S/X receiving systems, an LCP system would be optimal.

The third issue is the radiation pattern of the antenna itself. VLBI interferometers have an angular resolution of approximately λ/D, where λ is the observed wavelength and D is the distance between two telescopes of a baseline. Assuming a representative minimum frequency of 2 GHz and maximum frequency of 12 GHz (chosen for simplicity), the resolution of a 1000 km baseline is 150 and 25 nanoradian, and for a 5000 km baseline one fifth of this,

[1] (https://www.itu.int/).

respectively. At the altitude of a GNSS satellite of approximately 20 000 km, this amounts to 3 and 0.5 m for a 1000 km baseline and 0.6 and 0.1 m for the two example frequencies, respectively. These numbers demonstrate that the satellite antenna pattern will be resolved at least in the higher frequency range with consequences for the interferometer response. Similar to the so-called source structure effect of natural radio sources (Charlot, 1990), the antenna pattern will lead to source structure phase variations, which will have to be corrected in the *level 2 data analysis* of the VLBI data. For this purpose, the antenna needs to be calibrated preferably in an anechoic chamber (Görres et al., 2006) before its launch. From this calibration a field of phase correction values will be determined for a grid of relative positions in the (u, v)-plane (Thompson et al., 2017).

The last initial consideration, which we take into account for our concept, is triggered by a recent ESA call (European Space Agency, 2019). Here, a maximum power consumption and mass of the equipment to be considered are set to 3 W and 1–3 kg respectively. Staying within these limits may increase the chance for a realization of the concept proposed in the subsequent paragraphs.

3. The artificial signal

3.1. VLBI uncertainty requirements

The concept of the artificial satellite signal is the first element which needs to be defined before starting with the technical draft. It needs to meet a set of requirements to achieve a theoretical accuracy of the group delay for near-field satellite observations which is at level with the standard VLBI accuracy.

Geodetic and astrometric VLBI with quasars makes use of bandwidth synthesis (Rogers, 1970). The spanned bandwidth is sampled with a number of intermediate frequency (IF) sub-bands (8 or 10 in X band and 6 in S band) of up to 16 MHz width at a variety of intervals (Fig. 1). This results in an optimal delay resolution function which stems from the Fourier transform involved in processing the cross-power spectra of the correlation process. For more details see Nothnagel (2018).

The requirements for the artificial signal can be developed from the theoretical uncertainty σ_τ of the group delay observable for the standard quasar VLBI case (Thompson et al., 2017), which depends on the effective spanned bandwidth $\Delta\nu_{\mathrm{RMS}}$ of the receiving system and the signal to noise ratio (SNR),

$$\sigma_\tau = \frac{1}{2\pi \cdot \mathrm{SNR} \cdot \Delta\nu_{\mathrm{RMS}}}. \tag{1}$$

Increasing the SNR and/or the $\Delta\nu_{\mathrm{RMS}}$ yields a decrease of σ_τ which indicates better determination of the time delay. The effective bandwidth $\Delta\nu_{\mathrm{RMS}}$ is determined according to

$$\Delta\nu_{\mathrm{RMS}} = \sqrt{\frac{\sum_{i=1}^{n}(\nu_i - \bar{\nu})^2}{n}}, \tag{2}$$

where ν_i is the individual channel frequency, $\bar{\nu}$ is the mean frequency, and n is the number of channels.

The SNR is the ratio between the level of the signal to the level of the disturbing background noise and can be computed theoretically with

$$\mathrm{SNR} = \eta \frac{S}{2k_{\mathrm{B}}} \sqrt{\frac{A_{\mathrm{eff1}} \cdot A_{\mathrm{eff2}}}{T_{\mathrm{sys1}} \cdot T_{\mathrm{sys2}}}} \cdot \sqrt{2\Delta\nu T}, \tag{3}$$

where η is the digitizing loss factor (0.5–0.7), S is the correlated flux density of the radio source, k_{B} is Boltzmann's

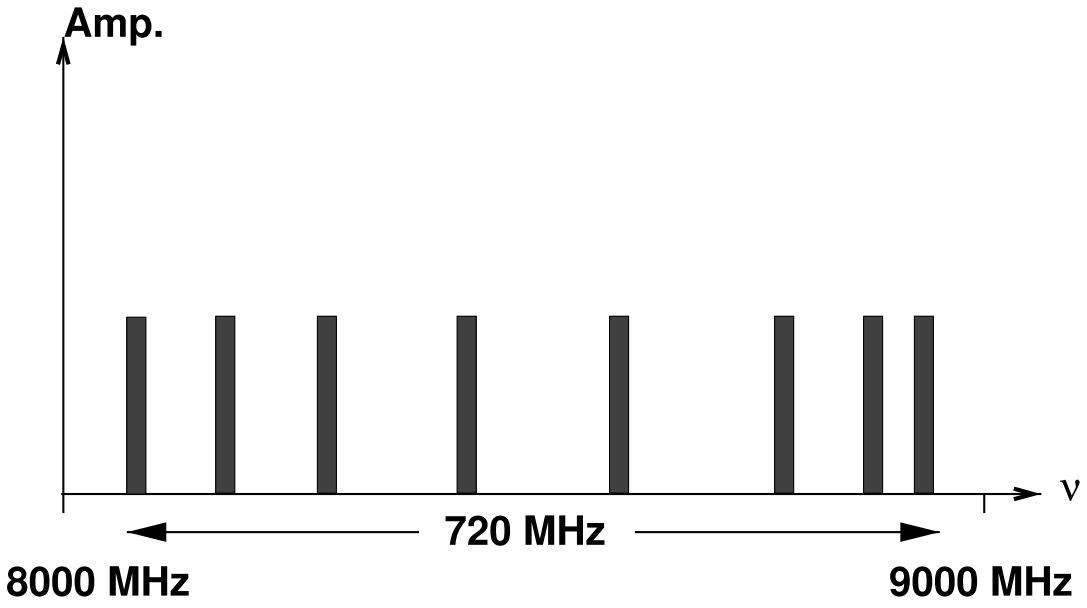

Fig. 1. Generic example of channel bandwidth and distribution at X band between 8000 and 9000 MHz. Channel bandwidths can be 4, 8 or 16 MHz.

constant, $A_{\mathrm{eff}i}$ is the effective antenna area of telescope i, $T_{\mathrm{sys}i}$ is the noise temperatures of the receiving system i, Δv is the total bandwidth of the receiving system (n times the channel bandwidth), and T is the coherent integration time.

The uncertainty of standard (legacy) VLBI observations is about 20 ps, which is equivalent to a 6 mm path length. This can be derived from Eq. (1) applying Eq. (2) to the 8 channels normally spread over a bandwidth of 720 MHz at X band. The individual channel bandwidths and the integration time in Eq. (3) are normally chosen to meet SNR thresholds of 25–30. Channel bandwidths of up to 16 MHz are possible and the integration time can be up to several hundred seconds but should be limited to 60–100 s to achieve a great number of observations per hour in classical VLBI sessions.

Concerning the observations of near-field satellites the integration time should be even shorter to minimize the challenging effects of satellite movements. To be able to decrease the integration time, the satellite signal strength should be increased as compared to flux densities stemming from quasars which is mostly below 1 Jansky ($1\ \mathrm{Jy} = 10^{-26}\ \mathrm{W\ Hz^{-1}\ m^{-2}}$). An increase of up to approximately 10 Jy is considered reasonable for the time of initial investigations and testing but should be reconsidered to a lower bound when enough experience has been gained at a later stage. The limitation serves to avoid additional RFI as mentioned in Section 2, but even more importantly to allow observations of quasars and satellites within short time intervals but without the need for changing the observing setups.

For VGOS observations all these considerations apply in the same way. Here, the smaller antenna apertures are compensated for with wider bandwidths and nominally increasing the number of correlated samples by observing and registering two perpendicular linear polarization signal paths (Niell et al., 2018).

As a consequence of all of these considerations, it can be stated that on the GNSS satellite, a noise source should emit radiation, which covers the full band from 2 to 14 GHz. This allows both legacy and VGOS telescopes to observe the satellite and achieve group delay uncertainties at the same level as for quasar observations in short integration periods. An important factor is that these observations are possible with existing hardware setups at the radio telescopes on Earth. This increases the acceptance and willingness of radio telescope operators to include these observations in their routine schedules.

Sometimes modulated signals are proposed as an alternative concept. However, the processing of these signals with radio telescope signal chains would require additional components which would have to be designed and installed, a fact which would probably limit the usable radio telescopes quite severely.

3.2. Link budget

The next step is the determination of the required level of transmitted signal power. To compute this, the link budget has to be calculated, which is the total of gains and losses of the signal power from the transmitter (Galileo satellite) to the receiver (VLBI radio telescope) through the medium between them. The link budget consists mainly of the telescope gain and path losses (free path loss and atmospheric attenuation). The link budget equation is

$$\begin{aligned}\text{Transmitted Power [dB]} = {} & \text{Received Power [dB]} \\ & - \text{Gains [dB]} \\ & + \text{Losses [dB]}. \end{aligned} \tag{4}$$

3.2.1. Radio telescope gain

In radio astronomy, the radio telescope gain represents the relation between the antenna temperature and the flux density of the radio source (Marr et al., 2015):

$$\text{Telescope Gain}\ \left[\frac{\mathrm{K}}{\mathrm{Jy}}\right] = \frac{A_{\mathrm{eff}}}{2k_{\mathrm{B}}}, \tag{5}$$

where A_{eff} is the aperture efficiency, and k_{B} is the Boltzmann constant ($1.38\ 10^{-23}\ \mathrm{W\ s\ K^{-1}}$). It should be mentioned that in communication technology, the gain represents the transmitted/received power in a certain direction of an antenna compared to an isotropic antenna. In contrast to the gain in Eq. (5), the gain – in communication – is unitless.

In general, radio telescopes have a high level of gain. This can be calculated with the equation (Stutzman and Thiele, 2012):

$$\text{Telescope Gain [dB]} = 10\ \log_{10} k\left(\frac{\pi d}{\lambda}\right)^2, \tag{6}$$

where λ is the signal wavelength, d is the diameter of the telescope, and k is the efficiency factor, which is typically between 0.4 and 0.6. In Eq. (5), the gain is decreasing with frequency as it is a function of the efficiency, but in Eq. (6) it is increasing with frequency due to its relation with the wavelength. It is important to mention that the different gain behaviors with frequency, even though both equations are correct, is only due to the units.

As example for a VGOS system, Fig. 2 shows the gain for a radio telescope with 13.2 m diameter over the frequency range of 2–14 GHz with an average efficiency factor of $k = 0.5$ following Eq. (6). Since the efficiency factor normally decreases with increasing frequency, the graph is augmented with error bars representing the gain with efficiency factors of 0.6 and 0.4. In this regime, the error bars do not exceed 1 dB indicating that the efficiency factor only plays a secondary role in the gain considerations. Thus, the overall telescope gain increases towards higher frequencies.

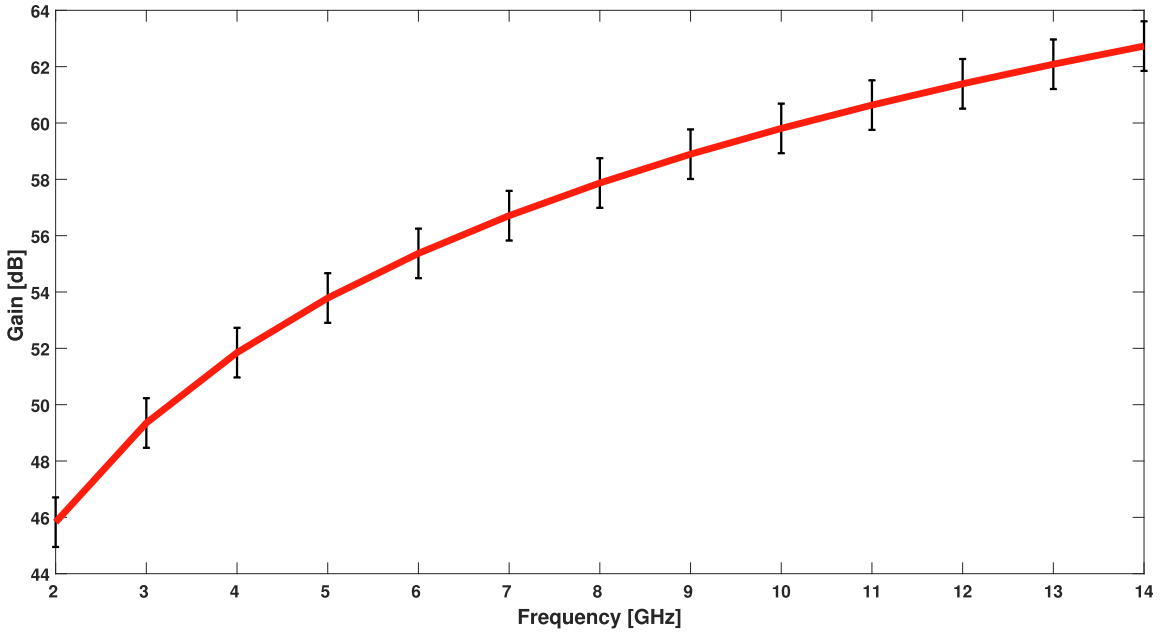

Fig. 2. Generic gain of a parabolic telescope with 13.2 m diameter over the frequency range 2–14 GHz with efficiency factor $k = 0.5$. Error bars represent variations in efficiency factor of ± 0.1. The gain of a telescope increases with increasing frequency, although the efficiency decreases. However, the latter effect is dominated by the increase in gain.

3.2.2. Path losses

While the signal is propagating through the medium between a satellite and a telescope, it will suffer from power attenuation due to Free-Space Path Loss (FSPL) and atmospheric attenuation. The FSPL is proportional to the distance and it can be calculated using the following expression (Anderson, 2003)

$$\mathrm{FSPL} = 32.44 + 20\ \log_{10}\ f_{\mathrm{MHz}} + 20\ \log_{10}\ D_{\mathrm{km}}, \qquad (7)$$

where D_{km} is the distance between the satellite and the radio telescope in km, and f_{MHz} is the frequency in MHz. The distance varies depending on the elevation angle ε of the telescope. In zenith direction, the distance corresponds to the satellite height, which is approximately 23,220 km for Galileo satellites. In the worst case, where the elevation angle ε is down to 5°, the distance will be much larger. Thus, the maximum distance d is 28,349 km, as computed with the following formula:

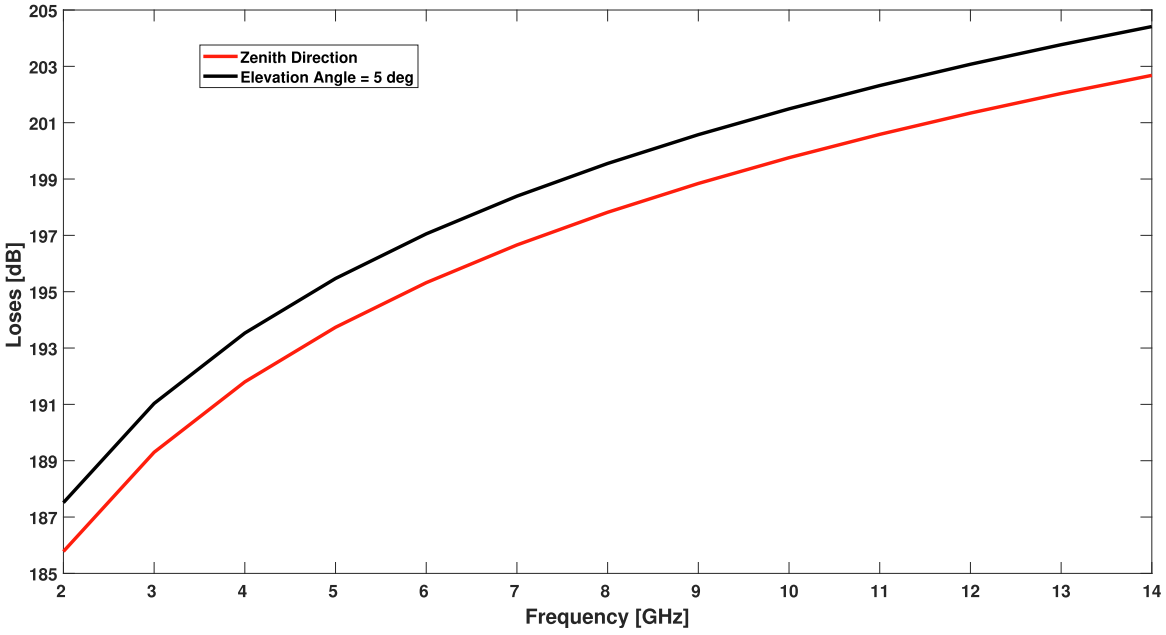

Fig. 3. Free-space path loss in the zenith direction (red line) and at $\varepsilon = 5°$ (black line) over the frequency range 2–14 GHz. The difference in FSPL at the highest and lowest frequency is about 17 dB. The elevation dependent effect is much smaller than the frequency dependent increase.

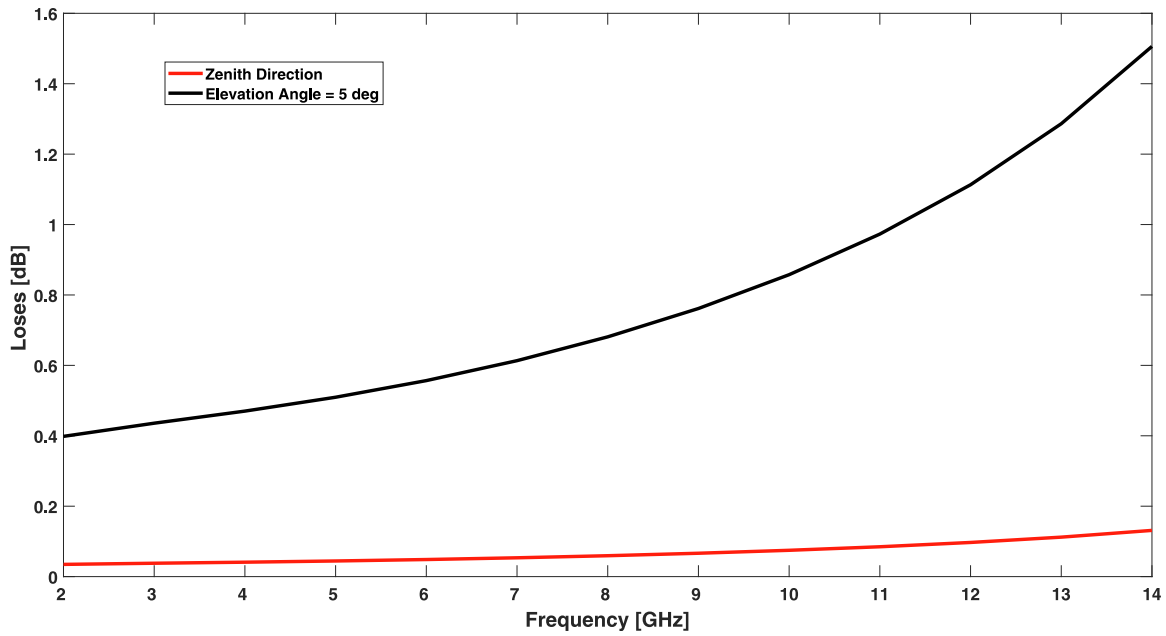

Fig. 4. Atmospheric attenuation in the zenith direction (red line) and at $\varepsilon = 5^\circ$ (black line) over the frequency range 2–14 GHz from the total link budget. The elevation dependent increase in loss is much more pronounced than that of the frequency dependency especially at the higher frequencies.

$$d = -R_E \sin\alpha + \sqrt{R_E \sin\alpha^2 + H^2 + 2HR_E}, \quad (8)$$

where R_E is the Earth radius, H is the satellite height, ε is the elevation angle.

In addition to the geometrical effect, the FSPL depends on the frequency. In Fig. 3 the loss is computed according to Eq. (7). The graph shows the FSPL for a signal emitted by a Galileo satellite and received from the zenith direction and with an elevation angle of $\varepsilon = 5^\circ$. As can be seen, the FSPL increases towards higher frequencies with only a slight effect of about 1–2% through the distance which depends on the elevation angle. The difference in FSPL at the highest and lowest frequency is about 17 dB.

The second origin of path loss is atmospheric attenuation, which depends on the meteorological circumstances. The atmospheric attenuation was estimated according to the ITU recommendations (ITU, 2013).[2] For the computations, we assume a total path length between telescope and clouds of 5 km in zenith direction (Karmakar et al., 2011) and 57 km at $\varepsilon = 5^\circ$. With standard atmospheric conditions of surface pressure at sea level of 1013 hPa and humidity of 7.5 g/m^3, we find a weak atmospheric attenuation, where the maximum attenuation in zenith direction is less than 0.2 dB and varies between 0.4 and 1.4 dB at $\varepsilon = 5^\circ$ (Fig. 4).

Then, Fig. 5 illustrates the necessary transmit power resulting from the total link budget for the assumed minimum flux density of 1 Jy to be received on Earth. From this graph, we conclude that the transmit power has to be at least −117 dBW/Hz, to ensure that the received flux density is at least 1 Jy at any VLBI frequency and elevation angle.

The increase in gain of the radio telescopes for higher frequencies is compensated for by the path loss and yields an almost constant link budget in zenith direction. Nonetheless, the link budget still varies by about 1.5 dB with respect to frequency at $\varepsilon = 5^\circ$ and by a maximum difference of about 3.5 dB between zenith and $\varepsilon = 5^\circ$. However, these variations are not problematic, but they have to be taken into account for designing the transmit antenna and choosing the amplifiers to keep the flux density received on Earth within the proposed range (1–10 Jy).

4. Equipment design

In this section, we draft the equipment, which will be necessary for generating an artificial signal for geodetic VLBI based on the assumptions and limitations mentioned above. This includes several electrical devices such as noise sources, amplifier, and transmit antenna. When selecting or designing these devices, the considerations taken into account are the power consumption, the gain and its flatness, in addition to the weight of each device and operating conditions, ensuring good performance in VLBI post-processing, and complying with ESA's call for idea specification. We will present an analysis of the performances and characteristics. The noise source and the amplifiers are available on the market. For this reason, we use the manufacturer's data sheets as the source of data. The antenna was designed and simulated for this particular purpose in order to guarantee good performance. At this stage, we are unable to provide characteristics in and suitability for space environment.

[2] ITU recommendations (ITU, 2013) has been superseded by (ITU, 2019), and it will be considered in future for further processing.

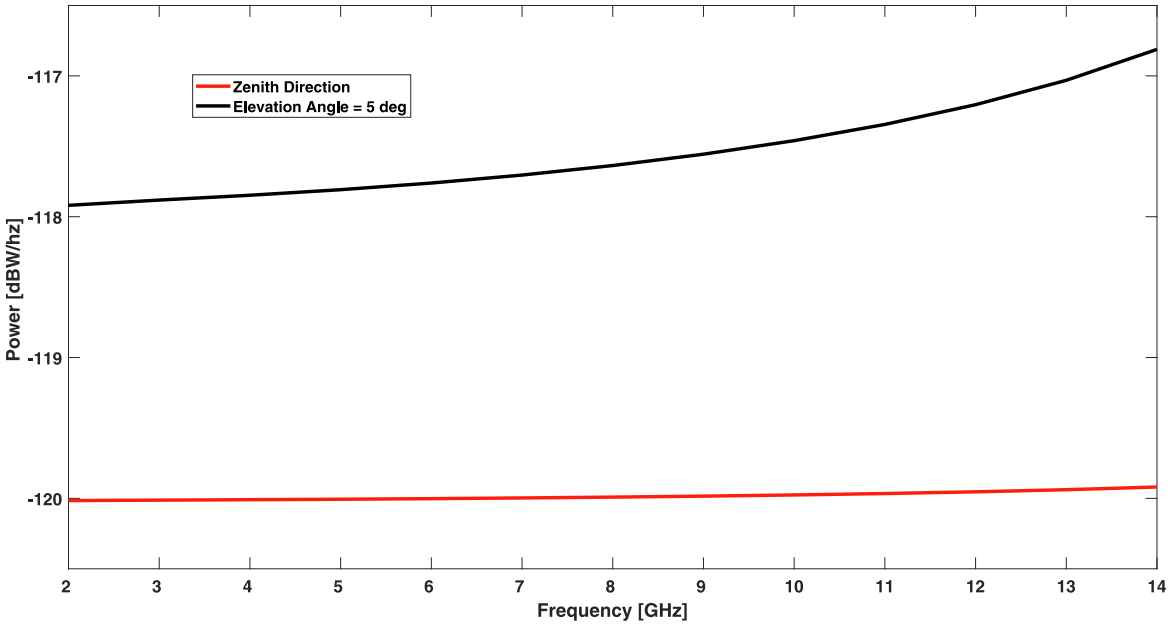

Fig. 5. Required transmitted power in the zenith direction (red line) and at $\varepsilon = 5°$ (black line) over the frequency range 2–14 GHz from the total link budget. The elevation dependent increase in loss is more pronounced than that of the frequency dependency especially at the higher frequencies resulting from the atmospheric attenuation.

4.1. Noise source

The noise diode was chosen from the catalog as it suits our purpose, more specifically the 346B noise source from KEYSIGHT[3] which emits noise from 0.1 to 18 GHz. The amplitude is defined in dBW/Hz (or dBm/Hz) or Excess Noise Ratio (ENR), where ENR is the ratio in decibel between the ON state of the diode and the thermal noise when the diode is OFF. In other words, ENR shows how much of the emitted noise exceeds thermal noise in terms of power. Thus, the intensity can be approximated by adding the ENR to the typical thermal noise level of −204 dBW/Hz at room temperature (Perez, 1998).

The ENR of the 346B noise source is around 15.2 dB with an 0.31 dB worst-case uncertainty and a root sum of squares uncertainty of 0.14 dB. For details about connector recommendations see the noise diode data sheet.[4] Obviously, the 346B noise source has a sufficient stability according to its manufacturer's data sheet (Fig. 6). The average current is 30 mA, and the voltage is ±28 V, thus, the power consumption is 0.84 W. The operating temperature is 0 to 55°C. The dimensions of the diode are: $140 \times 21 \times 31$ mm^3, and the weight is 0.1 kg.

4.2. Satellite antenna

Before we can deal with the amplifiers we have to know what the transmit antenna will look like. Considering the antenna, we have to bear in mind that the produced signal needs to have a considerably broad bandwidth from 2 to 14 GHz. Ideally, one would install the same type of feed horn on the satellite as in the VGOS radio telescopes, such as a Quadruple-Ridged Flared Horn style (Niell et al., 2018). However, this appears to be too large to be accepted by any space agency. For this reason, we propose to design a frequency independent antenna with the shape of a spiral. It should be mentioned as a sideline, that a circular polarized log-spiral antenna was also proposed for wideband astronomical observations at the end of our project (Abdalmalak et al., 2020).

The advantage of a spiral antenna for our purpose is that its fractional bandwidth can be as much as 40:1, in other words, if the lower frequency is 1 GHz, the upper frequency could be up to 40 GHz without significant changes in radiation pattern and polarization (Klimya and Prakash, 2015). Furthermore, the geometry of the spiral antenna is characterized by angle rather than by linear dimension, thus, the antenna's size remains small (30 mm in diameter and 25 mm in height). For its simple design, circularly polarization and stable performance, a two arms Archimedean Spiral Antenna (ASA) was chosen (Fig. 7).

The dimensions are determined based on the lower frequency f_{low} and the upper frequency f_{high} following Eqs. (9) and (10) (Caswell, 2001),

$$r_2 = \frac{c}{2\pi f_{\text{low}}}, \tag{9}$$

$$r_1 = \frac{c}{2\pi f_{\text{high}}}, \tag{10}$$

[3] Keysight Technologies. https://www.keysight.com/us/en/home.html.

[4] https://www.keysight.com/en/pd-1000001299%3Aepsg%3Apro-pn-346B/noise-source-10-MHz-to-18-ghz-nominal-enr-15-db?cc=JO&lc=eng.

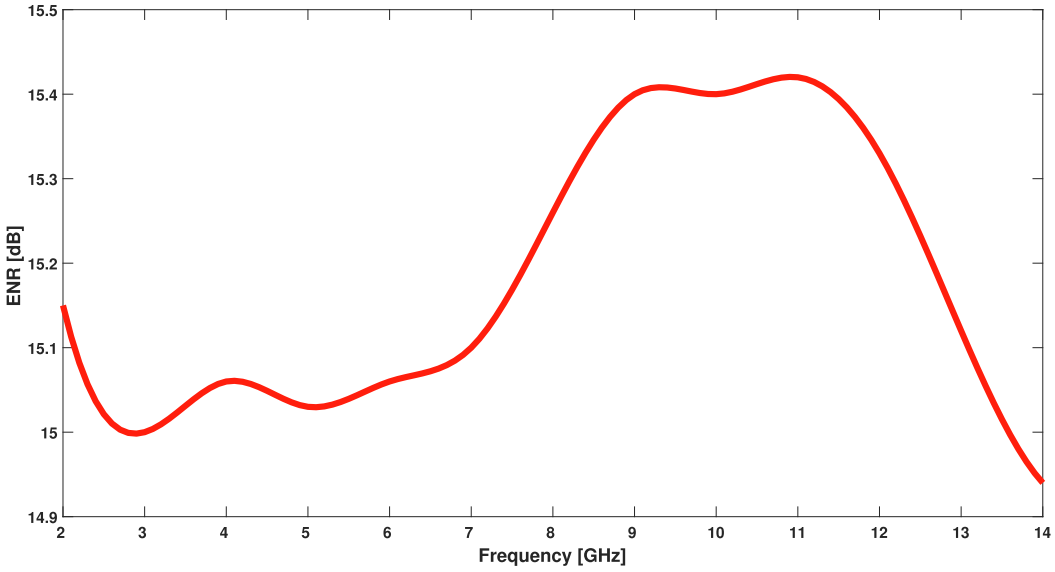

Fig. 6. Excess Noise Ratio (ENR) of the 346B noise source over the frequency range 2–14 GHz according to the manufacturer's data sheet. The ENR is around 15.2 dB with an 0.31 dB worst-case uncertainty and a root sum of squared uncertainty of 0.14 dB. It, thus, provides a sufficient stability across the spectrum to be observed.

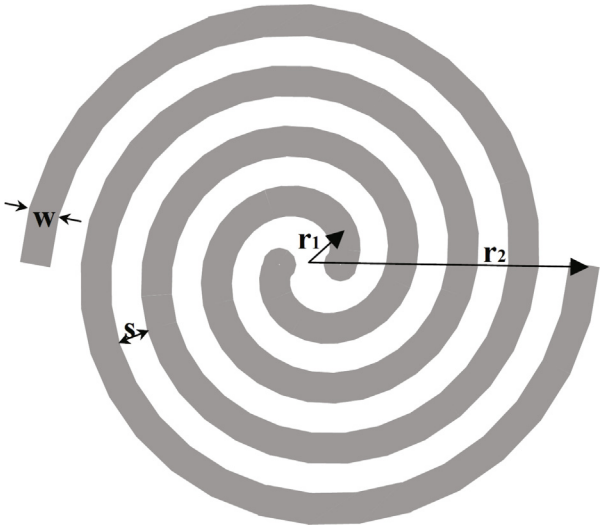

Fig. 7. Geometry of an Archimedean spiral antenna with wire width w, air region width s, inner radius r_1, and outer radius r_2 (Caswell, 2001).

where r_1 is the inner radius, r_2 is the outer radius, and c is the speed of light. As the ASA is a self-complementary antenna, the wire width w is equal to the air region width s. The wire width is proportional to the number of turns N according to:

$$w = \frac{r_2 - r_1}{4N}. \tag{11}$$

By following Babinet's principle, the input impedance of a self-complementary antenna in free space has to be 188.5 Ω (Caswell, 2001).

In most cases and particularly ours, the ASA has a bidirectional pattern that is undesirable as the rear radiation is reflected by the satellite itself back to Earth, which is troublesome for the VLBI post-processing. A cavity-backing is, therefore, used to make the pattern unidirectional with a high front-to-back ratio. Consequently, cavity-backing the antenna with an electromagnetic wave absorber is used, as it is recommended for high fractional bandwidth. However, this leads to a reduction in gain and increases the weight of the antenna depending on the design of the cavity-backing (Caswell, 2001). Another aspect is that the cavity-backing determines the polarization direction, either left or right hand circular polarization.

4.2.1. Antenna simulation

To construct the antenna and to simulate its behavior, the *ANSYS® HFSS™, Release 2020R2* software was used. The antenna was designed to work over the frequency range of 2–14 GHz which covers both the legacy S/X and the VGOS systems. However, the analysis was carried out in depth over the frequency bands used for the VGOS system. Currently, the receiving telescopes are set up for four 1 GHz broad bands of 3.0–4.0, 4.7284–5.7364, 8.5364–9.5444 and 9.5204–10.5284 GHz. The results, as shown later, are for the center frequencies of these bands, i.e., 3.5 GHz, 5.23 GHz, 9.04 GHz, and 10.02 GHz. The beamwidth of interest is $\alpha = [-14 - 14]$ according to

$$\alpha = \arctan\frac{R}{R + H}. \tag{12}$$

According to Eqs. (9) and (10), the inner and the outer radii are 3.4 mm and 23.9 mm, respectively. To ensure that the active region of the highest and lowest frequencies is located within the spiral arms, the inner and the outer radii

were set to be 2 mm and 27 mm, respectively. Each arm has four turns, and the wire width is 1.56 mm according to Eq. (11).

The absorber cavity-backing was also designed in the simulation environment. Four layers were mounted behind the antenna, one air layer and three layers of absorber material. The spiral and the absorber (dielectric) materials were placed in a one-side open stainless steel cylinder with outer radius of 30 mm and 1 mm thickness. Each absorber material has a different relative permeability ϵ_r and a dielectric loss tangent σ. The relative permeability ϵ_r is 1.1, 1.5, 2.0, and the dielectric loss tangent σ is 0.125, 0.25, 1.0 for the layers from top to bottom, respectively (Penney and Luebbers, 1994). The thickness of each copper layer is 6 mm, giving the cavity-backing a total depth of 25 mm (Fig. 8).

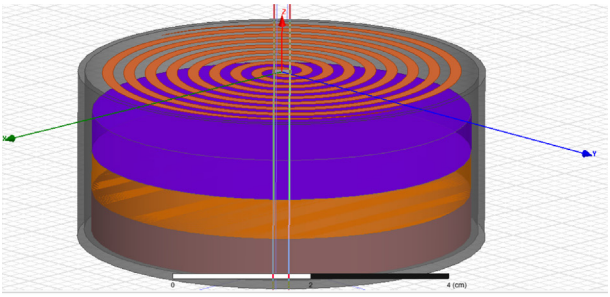

(a)

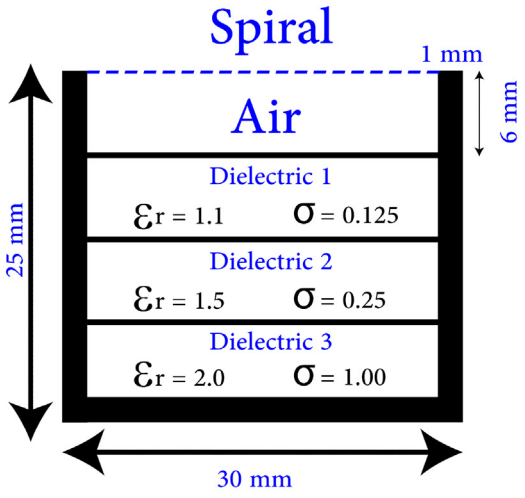

(b)

Fig. 8. Design of cavity-backed Archimedean spiral antenna. (a) 3D; (b) Cross section of (a). Credit for software and graphics: ANSYS Inc.

4.2.2. Antenna characteristics

With the design come a number of special antenna characteristic parameters.

1. Voltage standing wave ratio (VSWR): The VSWR is the ratio of the maximum voltage to the minimum voltage on the transmission line. It is widely used to determine the input and output power efficiency. Ideally, VSWR is 1, which is impossible to be achieved. VSWR has to be less than 2 to be accepted in most applications, which means that the antenna radiates power more than 88.9% of the total incident power (Wang et al., 2015). As the simulated result in Fig. 9 shows, the VSWR curve is less than 2 at 2 GHz, and approaching 1 for the higher frequencies. We conclude that the designed antenna will have high efficiency and low return power.
2. Axial Ratio: The axial ratio is the ratio of orthogonal components of an electromagnetic wave. Two orthogonal electric field components, with the same amplitude and a phase difference of 90°, make up an ideal circularly polarized wave, thus the axial ratio is 1 (0 dB). In this way, the axial ratio determines the circular polarization's quality. In fact, it is impossible to build a perfect circularly polarized antenna (axial ratio $= 0$ dB), therefore, an axial ratio of less than 3 dB is accepted (Gao et al., 2013). Our design has a much lower axial ratio than 3 dB in nadir direction with numbers close to 1 at the higher frequencies. This means that the radiation is of high quality left circular polarization (Fig. 10).
3. Return Loss: Impedance mismatching between the transmission line impedance and the antenna impedance causes reflection/return of the signal power which is known as return loss (Poole and Darwazeh, 2015). The return loss should be not more than -10 dB (Gao et al., 2013). In our case, if connected by a transmission line with 188.5 Ω impedance, it is about -15 dB at 2 GHz and dropping down to less than -40 dB at about 4.8 GHz (Fig. 11). Beyond that, it starts increasing again to a maximum of about -25 dB. So, the return loss is very small, which indicates high efficiency.
4. Radiation Pattern: The radiation pattern of the antenna represents how the power is being radiated in spatial directions. This can be depicted in a graph showing the 2D radiated energy vs. elevation angle (θ) or azimuth angle (ϕ) (Gao et al., 2013).The following results (Fig. 12) show that the cavity-backing works properly by making the antenna radiation uni-directional rather than bi-directional. Moreover, the antenna has a stable radiation pattern at all VGOS frequencies. Note that all the results are for $\theta = 0$.
5. Efficiency: The antenna efficiency η is defined as the ratio between the incident power and the radiated power in the far-field region. The perfect antenna radiates 100% of the incident power, which is impossible to be achieved due to unavoidable losses of the power within the antenna as reflected in the transmission line or

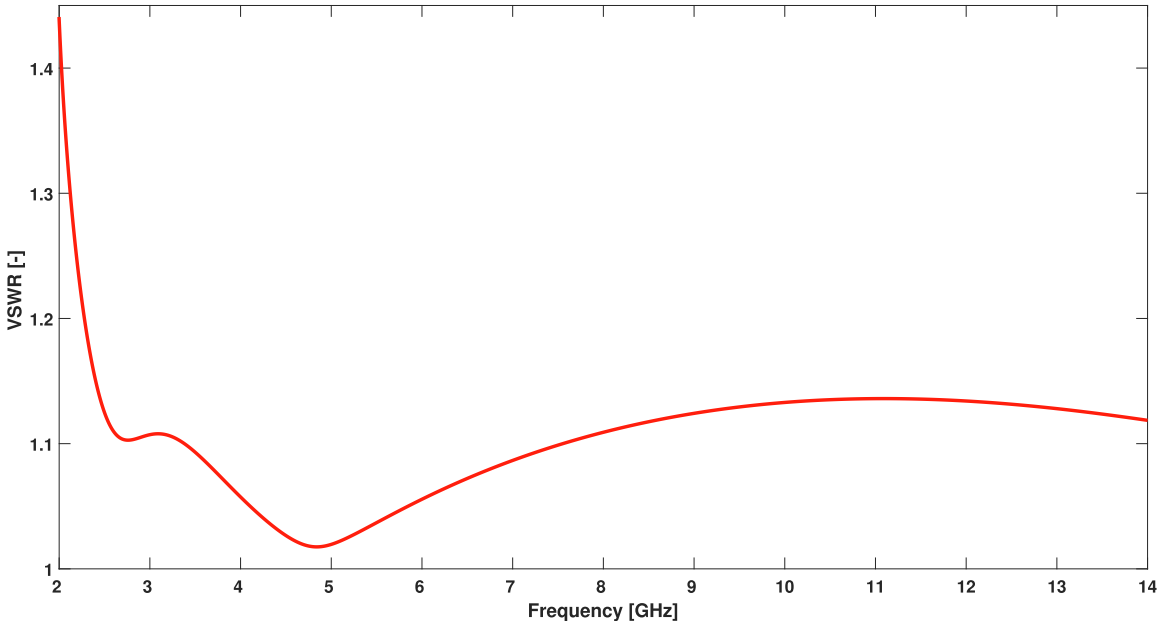

Fig. 9. Voltage Standing Wave Ratio (VSWR) of the Archimedean spiral antenna as a function of frequency, over the frequency range 2–14 GHz. Except of the first 500 MHz where there is a 30% increase in VSWR, the spectrum is stable within less than 10% variability.

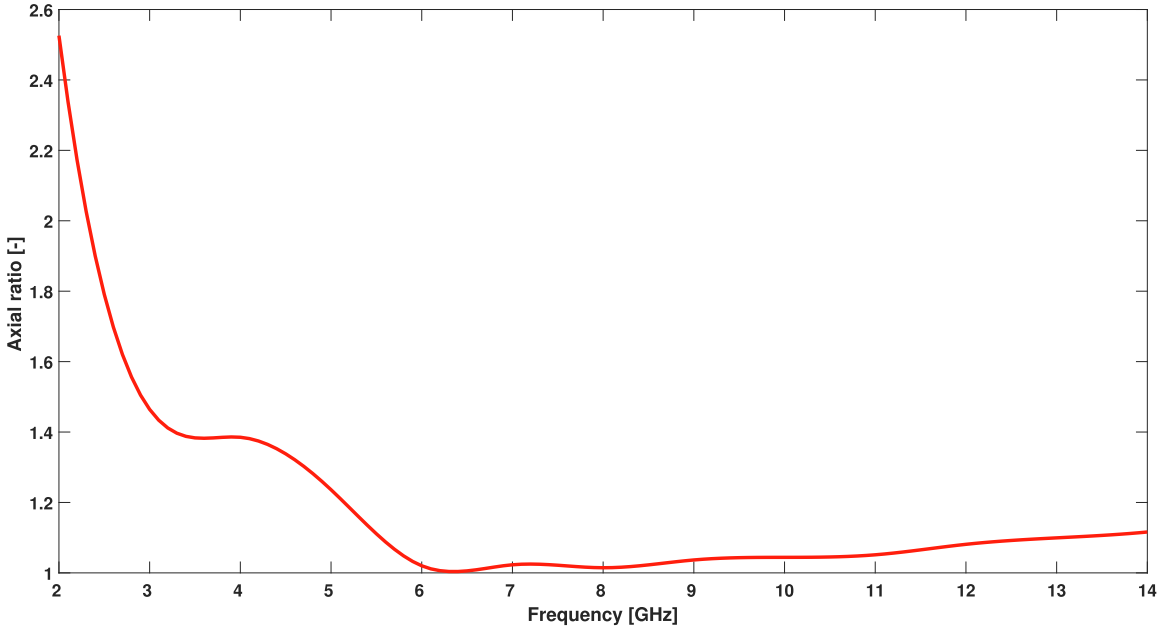

Fig. 10. Axial ratio vs. frequency, at antenna's elevation θ and azimuth angle $\phi = 0$, over the frequency range 2–14 GHz. With an acceptable ratio of < 3, the design is well suited for a transmitting antenna on the satellite.

absorbed by the antenna itself and converted to thermal energy. As previously seen, the antenna has a very low return loss, indicating high efficiency. The cavity-backing is, however, dampening the downward radiation. Therefore, one anticipates that the antenna efficiency is reduced, which is true for low frequencies (Fig. 13). In the case of higher frequencies, the simulation shows high efficiency. This behavior may be due to the cavity-backing not absorbing the reflected radiation in the lower frequency regime entirely. This is then reflected from the bottom of the cavity-backing, which was designed from stainless steel.

6. Gain: The antenna directivity D_v shows the radiated power of the antenna in a certain direction while the gain G is obtained by including the antenna efficiency in the directivity following Eq. (13). The gain can be cal-

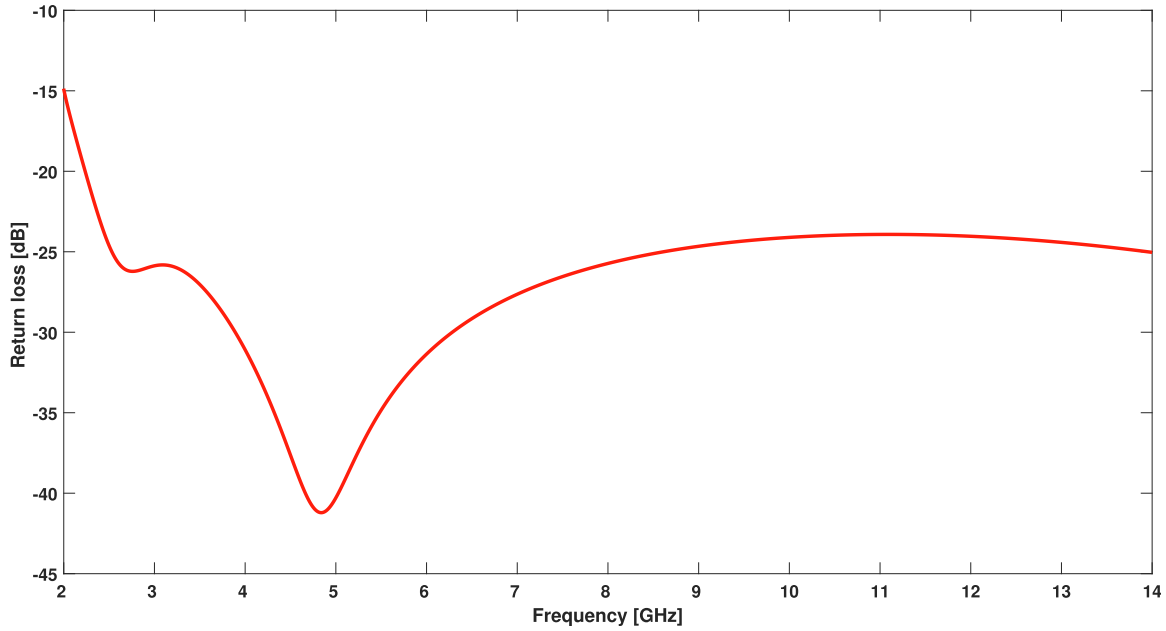

Fig. 11. Return loss vs. frequency, over the frequency range 2–14 GHz. These small losses indicate high efficiency of the antenna.

culated by comparing the measured transmitted power in a certain direction to the power transmitted by an isotropic antenna:

$$G(\theta,\phi) = \eta \cdot D_{\mathrm{v}}(\theta,\phi). \tag{13}$$

For our design, in the nadir direction the spectrum has a maximum gain at frequencies between 9 and 10 GHz and a minimum at 2 GHz (Fig. 14). At $\phi = 14^{\circ}$, the maximum is about 7.4 dB at 13 GHz and a minimum of about 2 dB at 2 GHz. The maximum difference in gain between nadir direction and $\phi = 14^{\circ}$ is about 0.7 dB at 8 GHz.

In conclusion to all these simulated parameters of the antenna, it can be stated that the design of the antenna shows excellent performance and stability, which should be adequate for the purpose of the equipment.

5. Amplifier

The last set of components to be designed are the amplifiers in between the noise source and the antenna. As shown earlier, the output signal power from the noise diode is about −188.8 dBW/Hz. With the antenna gain varying between ∼3–8 dB and an efficiency between 35% and 83%, the required transmit power should be −117 dBW/Hz. To achieve this, the signal has to be amplified based on the following expression:

$$\begin{aligned}&((\text{Noise Diode } [\text{dBW/Hz}] + \text{Amp } [\text{dB}])[\text{W/Hz}] \cdot \eta)\\ &\quad \times [\text{dBW/Hz}] + \text{Ant Gain } [\text{dB}]\\ &\quad = -117[\text{dBW/Hz}].\end{aligned} \tag{14}$$

Consequently, to get an output signal which gives rise to a flux density of at least 1 Jy, the signal has to be amplified with about 74 dB at 2 GHz and decreasing to around 65.5 dB at higher frequencies. Note that the unit's conversion between dBW and W in Eq. (14) has to be treated carefully.

A series of five low noise amplifiers was chosen with different gains to get the required total gain. Three different types were chosen from Analog Devices, Inc.[5] The criteria for choosing the amplifiers are ensuring the consistency between them, gain bias over lower frequencies, and low power consumption. The features of these amplifiers are shown in Table 1. However, other parameters have to be considered in future investigations, such as mean time between failures (MTBF), etc. (Lewis, 1995).

The combination of amplifiers, as listed in Table 1, has a low power consumption of about 1.4 W with each amplifier having a very small size. Moreover, this set balances the required gains over the full range of frequencies. All data are with the chips in a 50 Ω test fixture, which is suitable for the noise source. Fig. 15 shows the gain vs. frequency of the amplifier array. Nonetheless, based on the criteria above, different amplifiers combinations can be found and used.

6. Complete system

Fig. 16 presents a simple sketch of the proposed equipment with its items, i.e., the 346B noise source, amplifier array, Archimedean spiral antenna, and transmission lines with their impedances. The power consumption of the entire equipment is ∼ 2.24 W, the dimensions and the

[5] https://www.analog.com/en/index.html.

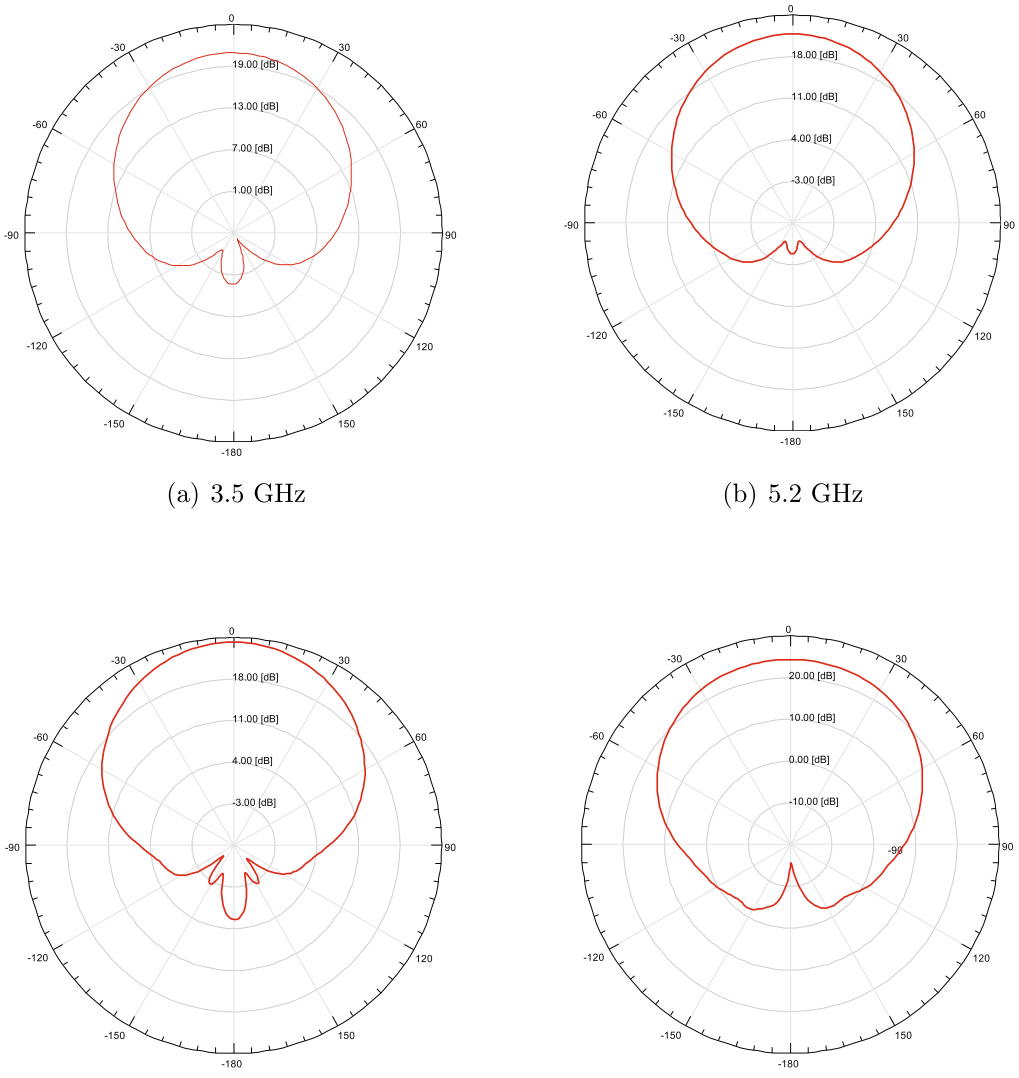

(a) 3.5 GHz (b) 5.2 GHz

(c) 9 GHz (d) 10 GHz

Fig. 12. 2D radiation patterns in dB at $\theta = 0$. 0° azimuth is the nadir direction of the antenna. (a) at 3.5 GHz; (b) at 5.2 GHz; (c) at 9 GHz; (d) at 10 GHz. The unwanted radiation towards the satellite are rather small but present nevertheless. Credit for software and graphics: ANSYS Inc.

weight of each device is small. The typical noise source and the amplifiers' operating temperature is 0–55 °C which needs to be controlled onboard the satellite. To save energy, the noise source and the amplifiers could be included in thermally controlled enclosures already existing on the satellite.

Finally, the sum of the ENR of the diode, the amplifiers gain, and the antenna gain shows the power spectrum of the output signal. Calculating the link budget for the individual frequencies, the power spectrum of the received signal by a VLBI radio telescope is determined. Fig. 17 illustrates the power spectrum of the signal after reception in the best case of emitting and receiving, i.e., emitting the signal in the nadir direction and receiving it from the zenith direction, and the worst case of emitting and receiving, i.e., emitting the signal at a nadir angle of 14° and receiving it from an elevation angle of 5°. The best case received flux density varies between ~ 2 and 5.4 Jy, in the worst case, it varies between ~ 1.25 and 2.8 Jy. In both cases, the flux density is within the proposed limits, i.e., 1–10 Jy.

The band of interest is 2–14 GHz. However, the proposed device operates at the frequency range 1–18 GHz. The out-of-band emissions are 1–2 GHz and 14–18 GHz, with considerably lower power than the band of interest. The lower out-of-band emission ceases at 1 GHz due to the dramatic drop in the antenna gain. The upper out-of-band emission ceases at 18 GHz, which is the upper limit of the operational range of the noise source. For the implementation of a new system on-board a satellite, electromagnetic compatibility (EMC) studies should be discussed with the satellite integrator engineers (Clayton, 2006).

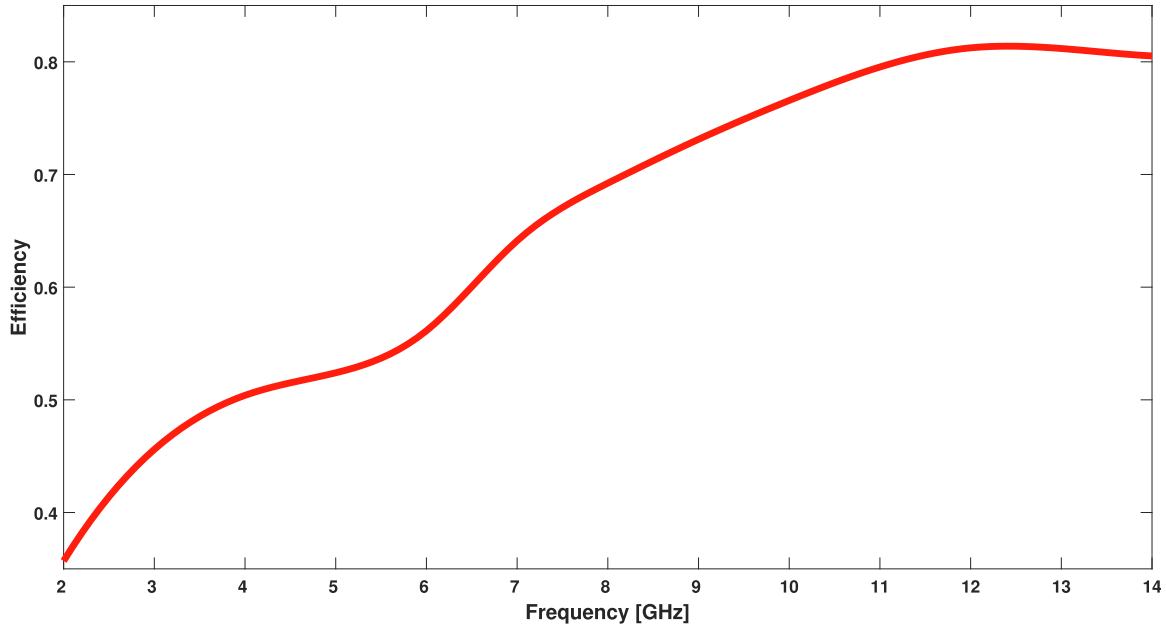

Fig. 13. Antenna efficiency vs. frequency over the frequency range 2–14 GHz. The lower efficiency at the lower frequencies may be due to the cavity-backing not absorbing the reflected radiation in this regime entirely.

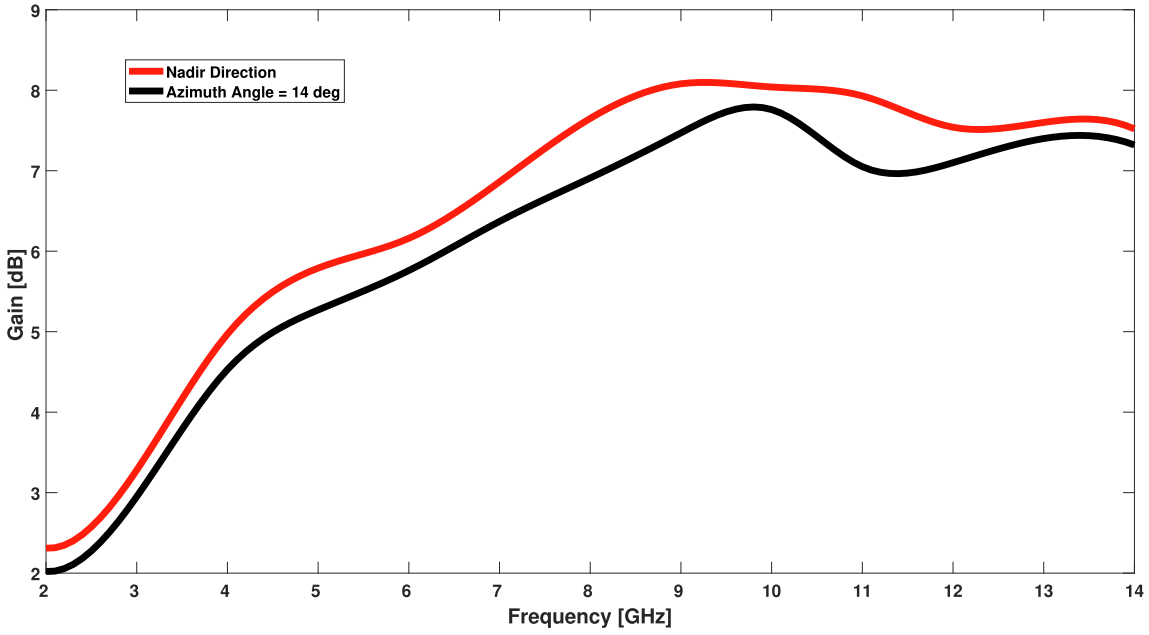

Fig. 14. Antenna gain vs. frequency. The Red line represents the antenna gain in the emitted in nadir direction, while the black line is at nadir angle = 14°.

Table 1
Amplifiers used in the simulations with their characteristics from manufacturer's data sheets.

Characteristics	HMC463LP5	HMC606	HMC-ALH482	Total/Common
Supply Voltage	+5 V @60 mA	+5 V @64 mA	+4 V @45 mA	–
Impedance Matching [Ohm]	50	50	50	–
Gain [dB]	12.3–13.5	12.8–15.1	15.8–16.1	67–75
Operating Temperature [C°]	−40 to +85	−55 to +85	−55 to +85	−40 to +85
Power Consumption [W]	0.3	0.32	0.18	1.4
Size [mm]	5 × 5	2.8 × 1.7	2 × 1.2	–
Operating Frequency [GHz]	2–20	2–18	2–22	2–18
No. of Amp.	1	3	1	5

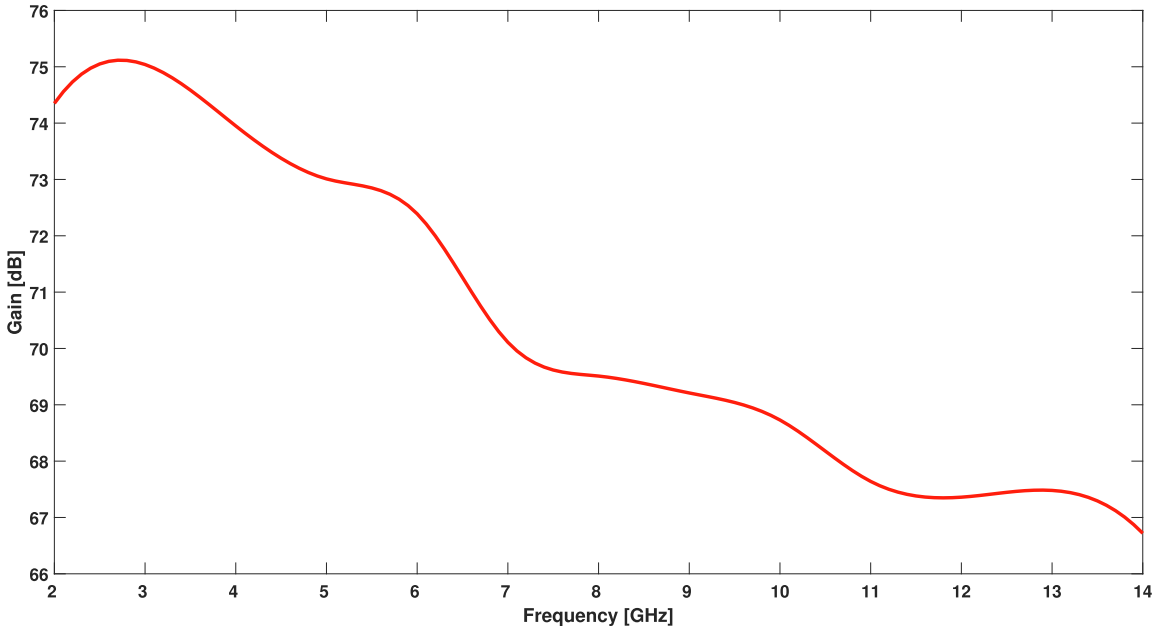

Fig. 15. Gain vs. frequency of the amplifier array over the frequency range 2–14 GHz. The gain deteriorates by about 8 dB towards the higher frequency nicely compensating for the lower antenna gain at lower frequencies.

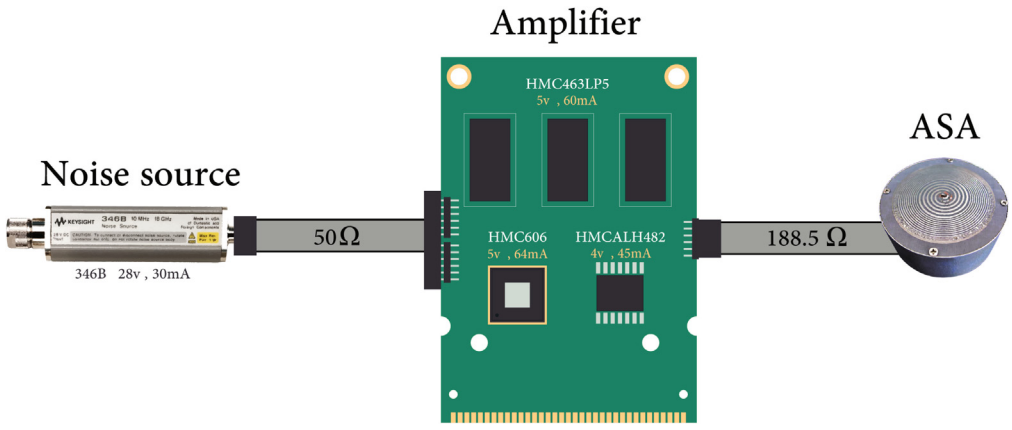

Fig. 16. A simple sketch of the VLBI signal generation equipment.

7. Raw data simulation and proof of concept

To test that the equipment can indeed be used for VLBI, the received noise is simulated and cross-correlated. For this purpose, the VLBI Baseband Data Simulator is employed (Gruber et al., 2021). The VLBI Baseband Data Simulator generates a VLBI baseband data stream which is the same as the output at a geodetic VLBI radio telescope. The model behind the noise generation contains realistic parameters of the telescope model, source characteristics, and velocities of sources and receivers. For more details and a full set of model parameters see Gruber et al. (2021).

In this section, two VLBI observation scenarios are simulated, correlated, fringe-fitted, and the results are compared. One scenario is based on the observation of a quasar that emits radiation characterized by a flat power spectrum which represents a default quasar observation in our study. In the second scenario, the observation of the presented VLBI transmitter with a power variation over frequency is simulated as described in Section 6. Hence, it is possible to compare the correlation and fringe-fitting results obtained from a default quasar observation with the results obtained from observation of the VLBI transmitter. Furthermore, this comparison study serves as proof of concept for the VLBI transmitter observation in a real processing chain.

To investigate the impact within the broadband frequency spectrum, a VLBI observation of two radio telescopes, forming a single baseline, observing with a standard broadband VGOS setup is simulated consisting of four frequency bands that comprise 32 channels each between 3 and 11 GHz. The VGOS frequency band labels and their corresponding frequency ranges are shown in Table 2. The bands are assigned in such a way that a pre-

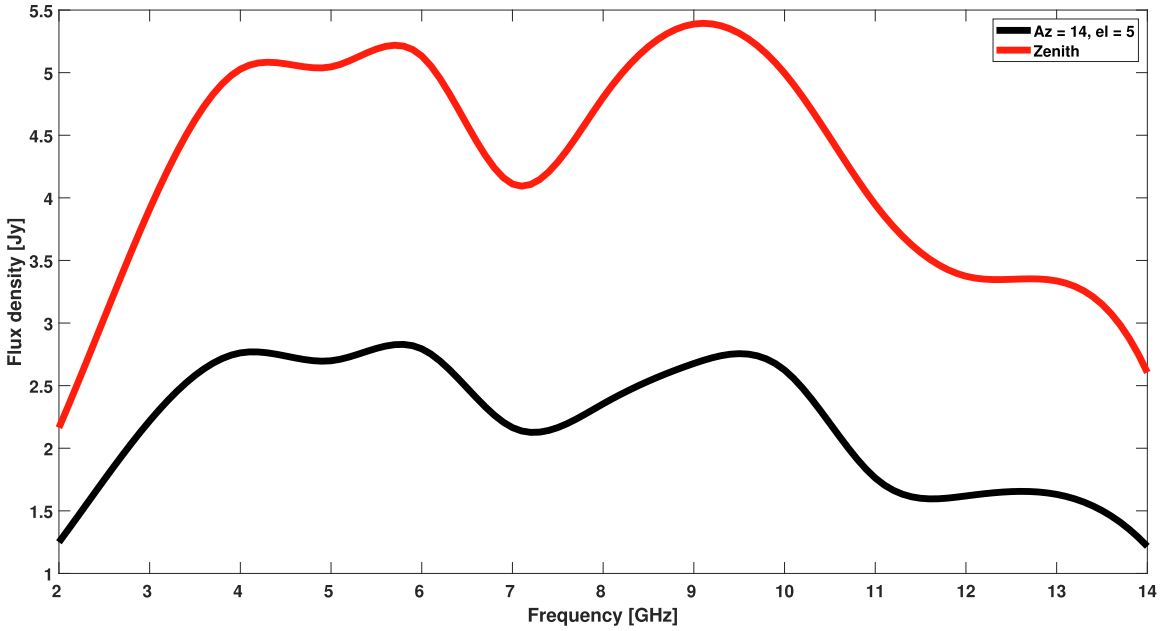

Fig. 17. Power spectrum of the signal as it will be received on Earth. Signal received from zenith of radio telescope (red line). Signal received from 5° elevation angle. On average the spectrum of the flux density is flat enough to allow successful VLBI observations with existing equipment.

cise and accurate (unambiguous) estimate of the multiband delay and the differential total electron content is possible, but other practical considerations are also taken into account that lead to the frequency band assignment currently in use (Petrachenko et al., 2009). The focus of the raw data simulation is to test the signal processing feasibility in a real VLBI processing chain. There is no particular scheduling or study to evaluate the visibility of the satellite by radio telescopes included. It is focused on the performance of the distinct power spectrum of the satellite in comparison to a default quasar observation with a flat power spectrum.

The raw data are sampled with 64 MHz and quantized with 2 bit which represents a standard VGOS observing mode. The observation duration for the simulation is set to 1 s and the station sensitivities for both stations are set to 1000 Jy. The flux density of the quasar is set to 10 Jy with a flat power spectrum across all bands.

In contrast, the observation of the VLBI transmitter is based on a distinct power distribution over frequency as described in Section 6. The power variation over frequency is applied with an arbitrary magnitude filter implemented in the simulation software (Gruber et al., 2021). Furthermore, a scenario which can be accomplished by a zero-baseline configuration is selected. The VLBI transmitter observation simulation is realized with a signal received in a good constellation, i.e., the signal is emitted in the nadir direction and received from the zenith direction for both telescopes. This simulation configuration has the advantage, that both telescopes receive the same amount of power.

Then, the signals are correlated using the DiFX software correlator (Deller et al., 2011) run on the Vienna High-Performance Computer Cluster (VSC-4). Fringe-fitting is carried out using fourfit.[6] The concatenation of both software packages represents the processing chain for correlation and fringe-fitting of real VLBI observation data. Thus, it is possible to investigate the processing feasibility of data received by the artificial VLBI transmitter in the real processing chain. For comparison, the interferometric amplitudes and phases within the four VGOS frequency bands obtained by DiFX correlation for quasar and satellite observations are presented in Fig. 18.

We notice that the power variations of the emitted radiation by the VLBI satellite transmitter are reflected in the amplitude values of the correlation product as well. A further inspection of the phases of the correlation product shows that the amplitude variations do not influence the phase estimation obtained by correlation. In fact, the phases are very stable around zero for all frequency bands and do not differ from the phases of the quasar observation. Hence, a difference for the interferometric phases cannot be found between the quasar observation and the observation of the presented VLBI transmitter.

Table 2
Label and frequency range of four VGOS frequency bands used in the simulation study.

Band	Frequency range (MHz)
A	3032.4–3480.4
B	5272.4–5720.4
C	6392.4–6840.4
D	10232.4–10264.4

[6] https://www.haystack.mit.edu/tech/vlbi/hops.html.

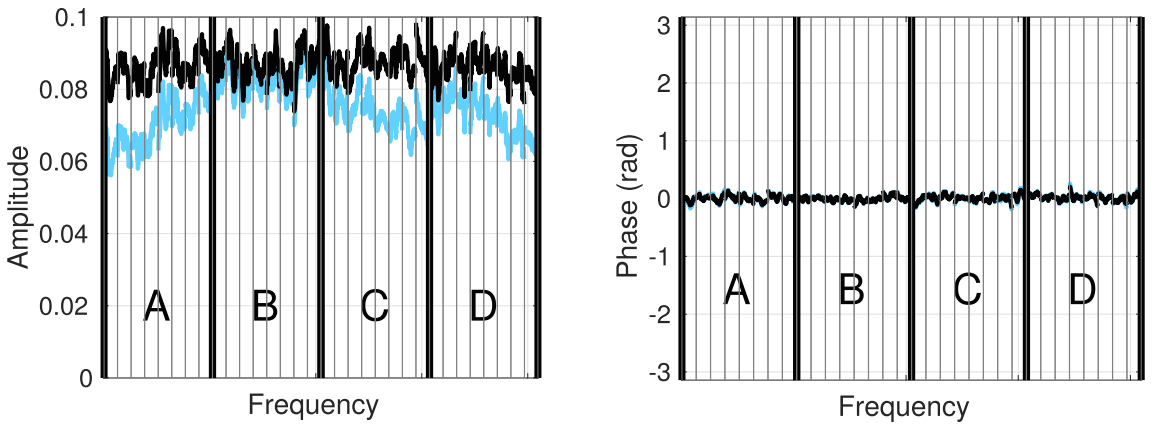

Fig. 18. The interferometric amplitudes (left) and phases (right) obtained by the DiFX correlation are depicted. The amplitudes and phases of the quasar observation are shown in black color, whereas the amplitude and phases of the VLBI transmitter observation are shown in blue color. The interferometric amplitudes (blue) reflect the power variation over the broadband spectrum of the VLBI transmitter and differ w.r.t the flat quasar spectrum. However, the interferometric phases (blue is covered by black phase values) do not show a systematic behavior for the VLBI transmitter observation and are stable across all four VGOS frequency bands (A: 3032.4–3480.4 MHz, B: 5272.4–5720.4 MHz, C: 6392.4–6840.4 MHz, and D: 10232.4–10264.4 MHz).

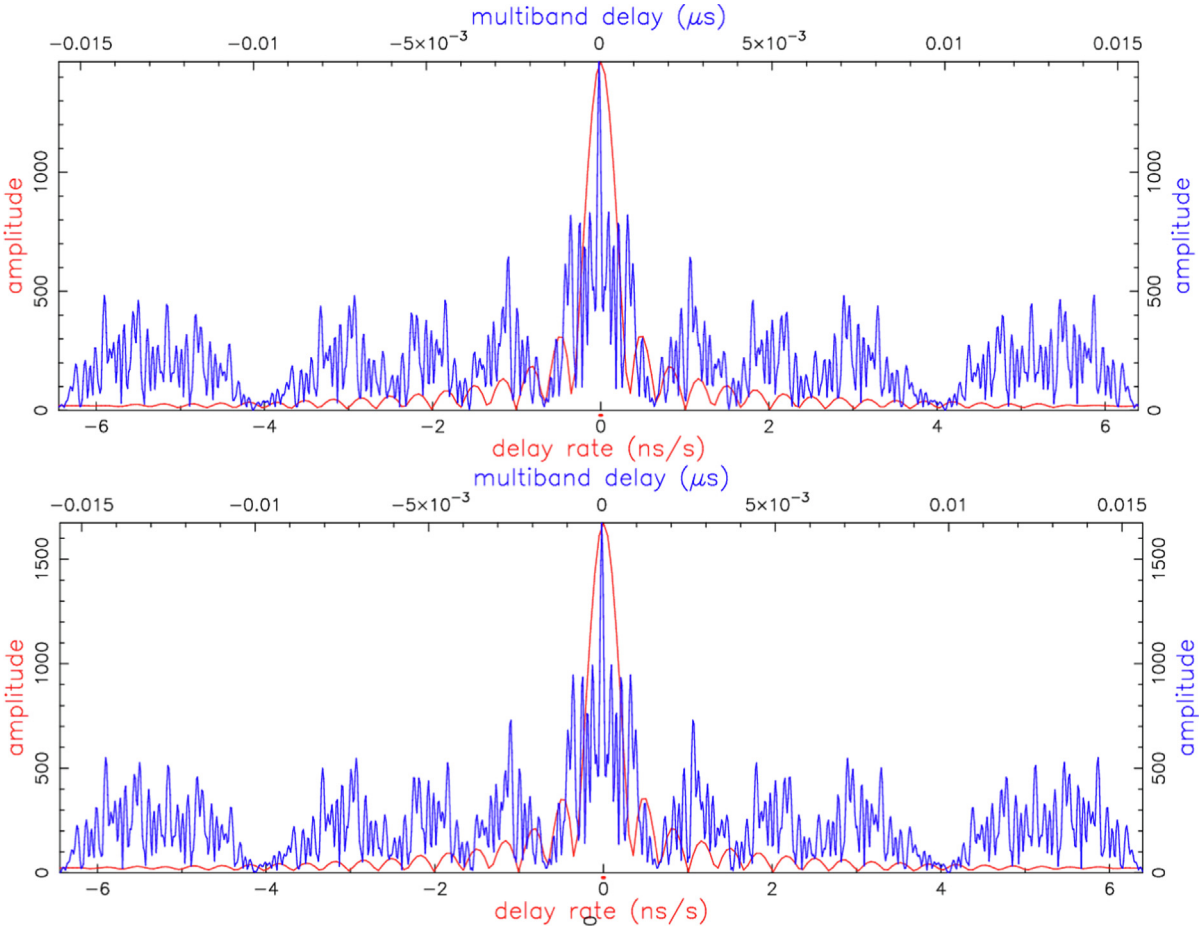

Fig. 19. The group delay function, also referred to as multiband delay function (blue color), obtained by fourfit fringe-fitting of the VLBI transmitter observation is shown (top) and of a quasar observation with a flat power spectrum (bottom). In addition, the delay rate function is depicted in red color. Both functions show a distinct peak. Hence, the group delay and the delay rate can be estimated precisely for the VLBI satellite transmitter observation, likewise for the quasar observation.

In a further investigation, the simulated observation data of the VLBI transmitter are fringe-fitted by the use of the fourfit software package. In general, the main goal of fringe-fitting is to estimate a group delay function for the entire broadband VGOS frequency setup. A sharp and unambiguous peak of the group delay function is desired to determine the group delay accurately. For this purpose the simulated raw data for the observation of the VLBI transmitter are fringe-fitted, and the resulting group delay function is shown in Fig. 19. The group delay function (blue color) depicted in the delay domain shows a sharp peak and reflects the characteristic shape as it is the case for a quasar observation with flat power distribution. Hence, the broadband signal provided by the VLBI transmitter can be used in the correlation process and for fringe-fitting to obtain the most important observable for geodetic VLBI, the group delay. In addition, the delay rate function is plotted in red color as well and shows a distinct peak without any systematic influences.

The group delay function (blue color) between the VLBI transmitter signal and the quasar signal differs marginally. This insignificant difference shows that the distinct power distribution of the VLBI transmitter signal does not affect the shape of the group delay function. Thus, similar group delay qualities derived from fringe-fitting can be obtained by the VLBI transmitter and the quasar.

8. Conclusions

Recently, tracking near-field satellites with VLBI has been receiving more and more attention in the geodetic community, and it is attracting the space agencies' interest to better link the dynamical reference frame of satellite orbits to the quasi inertial reference frame of natural radio sources. In order to link the respective frames, co-location of space-geodetic techniques are essential. They can be realized on Earth as so-called local ties or in space as space ties where two or more techniques are linked on the same spacecraft. What is still missing is a dedicated link between space geodetic satellite techniques and VLBI where a direct link between the satellite systems and the quasi-inertial reference frame realized by positions of extra-galactic radio sources can be established.

In view of the fact that there is no satellite emitting an optimal signal for VLBI observations, we presented a conceptual design for a dedicated VLBI transmitter to be installed on one or more Galileo satellites. Special care is taken that the signal matches the observing capabilities of the IVS both for the legacy S/X systems and the modern VGOS broadband systems. In addition, some considerations are documented which have to be taken into account when realizing the equipment on a satellite such as ITU legal aspects or pollution of the electromagnetic spectrum which is important for astronomy and astrophysics. Furthermore, some technical challenges were addressed, such as leaking the GNSS signal into the amplifier of the VLBI transmitter and observing the GNSS out-of-band emission when pointing at the satellite.

Table 3
Summary of suggested characteristics of the VLBI transmitter signal.

Signal Characteristics	Value
Frequency Range	2–14 GHz
Transmitted Power	−117 dBW/Hz
Received Flux density	1–5.5 Jy

The signal itself was designed to mimic the quasars' radiation, i.e., white noise, as closely as possible. Conceptually, three different devices need to be considered in the signal generation equipment, which are a noise source, amplifiers, and transmit antenna. The 346B noise source from KEYSIGHT was chosen due to its stable power spectrum and low power consumption. The antenna was newly designed to emit a broadband signal. For this purpose, a two arm Archimedean Spiral Antenna (ASA) was chosen. In terms of the results, equipment simulations showed stable performance with low return loss, relatively high gain, and good efficiency. However, before these devices can be deployed, they of course have to be tested in the laboratory, and other parameters have to considered as well such as failure rate or MTBF.

The signal characteristics were set to have a receiving flux density of 1–10 Jy resulting in an estimated transmit power of −117 dBW/Hz. After the link budget computations with Free-Space Path Loss (FSPL), atmospheric attenuation, and VLBI radio telescope gain, the flux density to be received on Earth varies between 2 and 5.5 Jy at zenith and between 1 and 3 Jy at an elevation angle of 5°, see Table 3.

In addition, raw data simulation with subsequent correlation and fringe-fitting were carried out. In this simulation an artificial signal, emitted from a Galileo satellite and received under extreme geometries by two radio telescopes, was generated with the VLBI Baseband Data Simulator (Gruber et al., 2021). Correlating and fringe-fitting these data showed a very similar performance for these signals as for signals from quasars. This documents that the overall approach is valid and can be used as a basis for further investigations in this topic. Extending the analysis to an end-to-end simulation, including final parameter estimation also taking into account the foreseen VGOS accuracy/precision goals should be part of future investigations. Finally, we should stress again that to protect radio astronomical observations, careful investigations of possible adverse effects on these observations are advisable and necessary.

Declaration of Competing Interest

The authors declare that they have no known competing financial interests or personal relationships that could have appeared to influence the work reported in this paper.

Acknowledgements

We thank Alex Dunning, Richard Porcas, and Sener Türk for useful discussions about antenna characteristics. Figs. 8a and 12 used courtesy of ANSYS, Inc. The computational results presented have been achieved in part using the Vienna Scientific Cluster (VSC). This research was funded in whole, or in part, by the Austrian Science Fund (FWF) [P31625]. We also thank FWF for funding open access of the publication.

References

Abdalmalak, K.A., Pantaleev, M., Garcia-Munoz, L.E., Santamaria, Botello G., Llorente-Romano, S., Rivera-Lavado, A., Flygare, J., Lopez Fernandez, J.A., Serna Puente, J.M., Garcia-Castillo, L.E., Segovia-Vargas, D., 2020. Ultrawideband Conical Log-Spiral Circularly Polarized Feed for Radio Astronomy. IEEE Trans. Antennas Propag. 68 (3), 1995–2007.

Altamimi, Z., Rebischung, P., Metivier, L., Collilieux, X., 2016. ITRF2014: A new release of the International Terrestrial Reference Frame modeling nonlinear station motions. J. Geophys. Res. Solid Earth 121 (8), 6109–6131.

Anderson, H.R., 2003. Fixed broadband wireless system design. John Wiley and Sons.

Anderson, J.M., Beyerle, G., Glaser, S., Liu, L., Männel, B., Nilsson, T., et al., 2018. Simulations of VLBI observations of a geodetic satellite providing co-location in space. J. Geodesy 92 (9), 1023–1046.

Bar-Sever, Y., Haines, B., Bertiger, W., Desai, S., Wu, S., 2009. Geodetic Reference Antenna in Space (GRASP) - A Mission to Enhance Space-based Geodesy. COSPAR Colloquium: Scientific and Fundamental Aspects of the Galileo Program, Padua, Italy. https://ilrs.gsfc.nasa.gov/docs/GRASP_COSPAR_paper.pdf.

Biancale, R., 2016. European Geodetic Reference Antenna in Space - European Reference Antenna of Space Geodetic Techniques Enhancing Earth Science (E-GRASP) - Eratosthenes, Proposal for Earth Explorer Opportunity Mission EE-9, Presented. In: First International Workshop on VLBI Observations of Near-field Targets, Institute of Geodesy and Geoinformation. University of Bonn, Bonn, Germany, http://www3.mpifr-bonn.mpg.de/div/meetings/vonft/pdf-files/talks/E-GRASP_Eratosthenes_Biancale.

Caswell, E.D., 2001. Design and Analysis of Star Spiral with Application to Wideb and Array with Variable Element Sizes. Doctor of Philosophy Dissertation. Virginia Polytechnic Institute and State University.

Charlot, P., 1990. Radio-source structure in astrometric and geodetic very long baseline interferometry. AJ 99, 1309–1326.

Charlot, P., Jacobs, C.S., Gordon, D., Lambert, S., de Witt, A., Böhm, J., Fey, A.L., Heinkelmann, R., Skurikhina, E., Titov, O., Arias, E.F., Bolotin, S., Bourda, G., Ma, C., Malkin, Z., Nothnagel, A., Mayer, D., MacMillan, D.S., Nilsson, T., Gaume, R., 2020. The third realization of the International Celestial Reference Frame by very long baseline interferometry. Astron. Astrophys. 644, A159.

Clayton, R.P., 2006. Introduction to electromagnetic compatibility, second ed. John Wiley & Sons Inc., Hoboken, ISBN: 978-0-471-75500-5..

Deller, A., Brisken, W., Phillips, C., Morgan, J., Alef, W., Capallo, R., Middelberg, E., Romney, J., Rottmann, H., Tingay, S., Wayth, R., 2011. Difx-2: a more flexible, efficient, robust and powerful software correlator. PASP 123, 275–287.

European Space Agency, 2019. H2020-ESA-038 GNSS Evolutions Experimental Payloads and Science Activities Call for Ideas, call issued on 08 February 2019. ESA Open Invitation to Tender AO9566, Open Date: 05/02/2019, Closing Date: 30/04/2019 13:00:00.

Gao, S.S., Luo, Q., Zhu, F., 2013. A Study on a Miniaturized Planar Spiral Antenna for Partial Discharge Detection in GIS. Circularly polarized antennas. John Wiley and Sons.

Görres, B., Campbell, J., Becker, M., Siemes, M., 2006. Absolute calibration of GPS Antennas: Laboratory results and comparison with field and robot techniques. GPS Solutions, vol. 10, number 2. Springer, pp. 136–145.

Gruber, J., Nothnagel, A., Böhm, J., 2021. VieRDS: A Software to Simulate Raw Telescope Data for Very Long Baseline Interferometry. Publ. Astron. Soc. Pac. 133 (1022), 044503.

Haas, R., Neidhardt, A., Kodet, J., Plotz, C., Schreiber, U., Kronschnabl, G., Yang, J., et al., 2014. The Wettzell-Onsala G130128 experiment-VLBI-observations of a GLONASS satellite. In: Behrend, Dirk, Baver, Karen D., Armstrong, Kyla L. (Eds.), IVS 2014 General Meeting Proceedings VGOS: The New VLBI Network. Science Press, Beijing, pp. 451–455.

Hamaker, J.P., Bregman, J.D., 1996. Understanding radio polarimetry. III. Interpreting the IAU/IEEE definitions of the Stokes parameters. Astron. Astrophys. Suppl. Ser. 117 (1), 161–165.

Han, S., Nothnagel, A., Zhang, Z., Haas, R., Zhang, Q., 2019. Fringe fitting and group delay determination for geodetic VLBI observations of DOR tones. Adv. Space Res. 63 (5), 1754–1767.

Hellerschmied, A., Böhm, J., Neidhardt, A., Kodet, J., Haas, R., Plank, L., 2015. Scheduling VLBI observations to satellites with VieVS. In: REFAG 2014. Springer, Cham, pp. 59–64.

Hellerschmied, A., Plank, L., McCallum, J., Sun, J., Böhm, J., 2016. In: Nothnagel, A., Jaron, F. (Eds.), Proceedings of the First International Workshop on VLBI Observations of Near-field Targets, October 5–6, 2016. Schriftenreihe des Inst. f. Geodäsie u. Geoinformation, vol. 54, Bonn, 1–6, ISSN 1864-1113. www3.mpifr-bonn.mpg.de/div/meetings/vonft/pdf-files/Proceedings2017.pdf.

Hellerschmied, A., McCallum, L., McCallum, J., Sun, J., Böhm, J., Cao, J., 2018. Observing APOD with the AuScope VLBI array. Sensors 18 (5), 1587.

ITU, 2013. Radio communication Sector of International Telecommunication Union, 2013. Recommendation ITU-R P.676-10: Attenuation by atmospheric gases. Electronic Publication, Geneva. https://www.itu.int/dms_pubrec/itu-r/rec/p/R-REC-P.676-12-201908-I!!PDF-E.pdf.

ITU, 2019. Radio communication Sector of International Telecommunication Union, 2019. Recommendation ITU-R P.676-12: Attenuation by atmospheric gases. Electronic Publication, Geneva. https://www.itu.int/dms_pubrec/itu-r/rec/p/R-REC-P.676-10-201309-S!!PDF-E.pdf.

ITU, 2020. Radio Regulations, Edition 2020. International Telecommunications Union, Geneva. http://handle.itu.int/11.1002/pub/814b0c44-en.

Jaron, F., Nothnagel, A., 2019. Modeling the VLBI delay for Earth satellites. J. Geodesy 93 (7), 953–961.

Karmakar, P.K., Maiti, M., Tech, M., Bhattacharyya, K., Angelis, C.F., Machado, L.A.T., 2011. Rain Attenuation Studies in the Microwave Band over a Southern Latitude. Pacific J. Sci. Technol. 12 (2), 196–205.

Klimya, T.S., Prakash, A.K., 2015. Cavity backing in spiral antennas. Int. J. Eng. Res. General Sci. Toc H Institute of Science and Technology, 3. Jg., Nr. 1.

Klopotek, G., Hobiger, T., Haas, R., Jaron, F., La Porta, L., Nothnagel, A., Zhang, Z., Han, S., Neidhardt, A., Plotz, C., 2019. Position determination of the Chang'e 3 lander with geodetic VLBI. Earth Planets Space 71 (1), 23.

Klopotek, G., Hobiger, T., Haas, R., Otsubo, T., 2020. Geodetic VLBI for precise orbit determination of Earth satellites: a simulation study. J. Geodesy 94 (6), 1–26.

Lewis, E.E., 1995. Introduction to Reliability Engineering, second ed. John Wiley & Sons Inc., Hoboken, ISBN: 978-0-471-01833-9.

Li, C., Liu, J., Ren, X., Zuo, W., Tan, X., Wen, W., Li, H., Mu, L., Su, Y., Zhang, H., Yan, J., Ouyang, Z., 2015. The Chang'e 3 mission overview. Space Sci. Rev. 190 (1), 85–101.

Männel, B., 2016. Co-location of geodetic observation techniques in space. Diss. ETH Zurich.

Marr, J., Ronald, L., Stanley, E., 2015. Fundamentals of Radio Astronomy: Observational Methods, vol. 13. CRC Press.

McCallum, J., Plank, L., Hellerschmied, A., Böhm, J., Lovell, J., 2016. Technical challenges in VLBI observations of GNSS sources. In: Nothnagel, A., Jaron, F. (Eds.), Proceedings of the First International Workshop on VLBI Observations of Near-field Targets, October 5–6. Schriftenreihe des Inst. f. Geodäsie u. Geoinformation, vol. 54, Bonn, pp. 17–22, ISSN 1864-1113, www3.mpifr-bonn.mpg.de/div/meetings/vonft/pdf-files/Proceedings2017.pdf.

Niell, A., Barrett, J., Burns, A., Cappallo, R., Corey, B., Derome, M., et al., 2018. Demonstration of a broadband very long baseline interferometer system: A new instrument for high-precision space geodesy. Radio Sci. 53, 1269–1291. https://doi.org/10.1029/2018RS006617.

Nothnagel, A., Artz, T., Behrend, D., Malkin, Z., 2017. International VLBI Service for Geodesy and Astrometry. Delivering high-quality products and embarking on observations of the next generation. JGeod 91, 711. https://doi.org/10.1007/s00190-016-0950-5.

Nothnagel, A., 2018. Very Long Baseline Interferometry. In: Freeden,W., Rummel, R. (Eds.), Handbuch der Geodäsie. Springer Reference Naturwissenschaften. Springer Spektrum, Berlin, Heidelberg doi: 10.1007/978-3-662-46900-2_110-1.

Penney, C.W., Luebbers, R.J., 1994. Input impedance, radiation pattern, and radar cross section of spiral antennas using FDTD. IEEE Trans. Antennas Propag. 42 (9), 1328–1332.

Perez, R., 1998. Wireless Communications Design Handbook: Interference into Circuits: Aspects of Noise, Interference, and Environmental Concerns. Academic Press.

Petrachenko, B., Niell, A., Behrend, D., Corey, B., Boehm, J., Charlot, P., Collioud, A., Gipson, J., Haas, R., Hobiger, T., Koyama, Y., MacMillan, D., Malkin, Z., Nilsson, T., Pany, A., Tuccari, G., Whitney, A., Wresnik, J., 2009. Design Aspects of the VLBI2010 System. Progress Report of the IVS VLBI2010 Committee.

Plank, L., 2014. VLBI satellite tracking for the realization of frame ties. Geowissenschaftliche Mitteilungen 95.

Plank, L., Böhm, J., Schuh, H., 2014. Precise station positions from VLBI observations to satellites: a simulation study. J. Geodesy 88 (7), 659–673.

Plank, L., Hellerschmied, A., McCallum, J., Böhm, J., Lovell, J., 2017. VLBI observations of GNSS-satellites: from scheduling to analysis. J. Geodesy 91 (7), 867–880.

Poole, C., Darwazeh, I., 2015. Microwave active circuit analysis and design. Academic Press.

Rogers, A.E.E., 1970. Very long baseline interferometry with large effective bandwidth for phase-delay measurements. Radio Sci. 5 (10), 1239–1247.

Rothacher, M. et al., 2009. The future Global Geodetic Observing System. In: Plag, H.P., Pearlman, M. (Eds.), Global Geodetic Observing System. Springer, Berlin, Heidelberg.

Stutzman, W.L., Thiele, G.A., 2012. Antenna theory and design. John Wiley and Sons.

Sun, J., Tang, G., Shu, F., Li, X., Liu, S., Cao, J., Hellerschmied, A., Böhm, J., McCallum, L., McCallum, J., Lovell, J., 2018. VLBI observation to the APOD satellite. Adv. Space Res. 61 (3), 823–829.

Thompson, A.R., Moran, J.M., Swenson, G.W., 2017. Introduction and Historical Review. In: Interferometry and Synthesis in Radio Astronomy. Astronomy and Astrophysics Library. Springer, Cham. https://doi.org/10.1007/978-3-319-44431-4_1, ISBN 978-3-319-44429-1.

Tornatore, V., Haas, R., Duev, D., Pogrebenko, S., Casey, S., Molera-Calves, G., Keimpema, A., 2011. Single baseline GLONASS observations with VLBI: data processing and first results. In: Proceedings of the 20th Meeting of the European VLBI Group for Geodesy and Astrometry, pp. 162–165.

Tornatore, V., Haas, R., Casey, S., Duev, D., Pogrebenko, S., Calves, G. M., 2014. Direct VLBI observations of global navigation satellite system signals. In: Earth on the Edge: Science for a Sustainable Planet. Springer, Berlin, Heidelberg, pp. 247–252.

Wang, Y., Li, J., Li, C., Ouyang, B., Zheng, Z., 2015. A Study on a Miniaturized Planar Spiral Antenna for Partial Discharge Detection in GIS. In: MATEC Web of Conferences, vol. 22, 02015. EDP Sciences.